A Comparison of Particle Tracking and Sizing Using Plenoptic Imaging and Digital In-line Holography

by

Elise Dahnke Munz

A thesis submitted to the Graduate Faculty of
Auburn University
in partial fulfillment of the
requirements for the Degree of
Master of Science

Auburn, Alabama
May 7, 2016

Keywords: plenoptic camera, digital in-line holography,
light field imaging, 3D PTV

Copyright 2016 by Elise Dahnke Munz

Approved by

Brian S. Thurow, Chair, Associate Professor of Aerospace Engineering
Stanley J. Reeves, Professor of Electrical Engineering
David E. Scarborough, Assistant Professor of Aerospace Engineering
Daniel R. Guildenbecher, Principal Member of the Technical Staff, Sandia National Laboratories

Abstract

Digital in-line holography and plenoptic photography are two techniques for single-shot, volumetric measurement of 3D particle fields. A preliminary comparison of the two methods is presented by applying plenoptic imaging to experimental configurations that have been previously investigated with digital in-line holography. These experiments include the tracking of secondary droplets from the impact of a water drop on a thin film of water and tracking of pellets from a shotgun. Both plenoptic imaging and digital in-line holography successfully quantify the 3D nature of these particle fields. This includes measurement of the 3D particle position, individual particle sizes, and three-component velocity vectors. For the initial processing methods presented here, both techniques give out-of-plane positional accuracy of approximately 1-2 particle diameters. For a fixed image sensor, digital holography achieves higher effective in-plane spatial resolutions. However, collimated and coherent illumination makes holography susceptible to image distortion through index of refraction gradients, as demonstrated in the shotgun experiments. In contrast, plenoptic imaging allows for a simpler experimental configuration. Furthermore, due to the use of diffuse, white-light illumination, plenoptic imaging is less susceptible to image distortion in the shotgun experiments. Additional work is needed to better quantify sources of uncertainty, particularly in the plenoptic experiments, as well as develop data processing methodologies optimized for the plenoptic measurement.

Acknowledgments

The work contained in this thesis could not have been completed without the help and support of numerous people. First, I would like to thank Dr. Brian Thurow for his extensive guidance in the completion of this research effort. I am exceedingly grateful for his efforts to help me develop both technical research skills and the communication and professional skills critical to successful science. I would also like to thank Sandia National Laboratories for the opportunity to conduct this research and especially Dr. Daniel Guildenbecher for his leadership in the execution of the experiments examined in this thesis as well as his work in digital in-line holography, which has provided the basis for the comparison presented here. I would like to thank Dr. Stanley Reeves and Dr. David Scarborough for their willingness to serve on my committee. I would like to thank the past and present members of the Advanced Flow Diagnostics Laboratory for their helpful technical discussions and especially their friendship during my time as a graduate student. Finally, I would like to thank my parents Larry and Lida Munz and my fiancé Taylor Hall for their support and encouragement of my education and for their continual reminders of the important things in life.

Table of Contents

List of Tables

List of Figures

List of Symbols

2D	two-dimensional
3D	three-dimensional
4D	four-dimensional
5D	five-dimensional
7D	seven-dimensional
AFDL	Advanced Flow Diagnostics Laboratory
LFIT	Light Field Imaging Toolkit
cm	centimeter
CCD	charge coupled device
d	particle diameter
c	circle of confusion
DIH	digital in-line holography
f	main lens focal length
Hz	Hertz
I_h	intensity of the interference
kg	kilogram
m	meter
mm	millimeter
MP	megapixel
ms	millisecond

ns	nanosecond
O	object wave
R	complex reference wave
s_i	image distance
s_o	object distance
U_r	reconstruction
x_l	resolution in the longitudinal direction
x_t	resolution in the perpendicular direction
μm	micron
μs	microsecond
λ	wavelength
Ω	effective angular aperture

I. Introduction and Background

The development of experimental diagnostics for non-invasive, instantaneous, three dimensional (3D) measurements of particle fields and flow phenomena is of interest for a wide variety of applications including quantification of 3D fluid flows [1], investigation of multiphase phenomena [2], [3], and explosion analysis [4]. To clearly motivate the necessity of these advanced diagnostics it is essential to understand the techniques they improve upon and the drawbacks of these earlier measurement methods.

Conventional diagnostic techniques to collect velocity, vorticity, and Mach number measurements include pressure based measurements and the use of thermal anemometry. The most common pressure based measurements involve the use of a Pitot probe or other pressure measurement probe and the Bernoulli equation to determine fluid velocity. These are inherently intrusive techniques and therefore care must be taken in the experimental implementation to use these finite sized probes in a manner which does not significantly affect the accuracy of the data collected. Additionally, it should be noted that pressure based measurements provide pointwise measurement values only at the locations where probes are located, therefore, to collect data from many locations in a flow, a large number of probes or some repetitive traversing mechanism must be implemented. Thermal anemometry involves a small heated wire placed in the fluid flow. The wire is made of a material which has a known dependence on temperature. The heat transfer from the wire as the fluid moves past the sensor is measured and can be used to obtain the velocity at that location. Like pressure based measurements, these techniques are invasive to the flow and result in point measurements at the location of the sensor [5].

Due to the complexities and possible inaccuracies associated with intrusive flow measurements, non-invasive optical techniques have become increasingly popular, first providing two dimensional (2D) measurements and eventually developing to provide 3D flow information. Particle based methods, in which the fluid flow is seeded with small particles which move with the fluid motion, are among the most popular optical techniques. Of interest in this work specifically is particle tracking velocimetry (PTV) in which the motion of individual particles is tracked between multiple images captured at known time steps. The matching of particles between frames has been accomplished using a variety of different imaging processing algorithms [5].

Historically, 2D techniques have been extended to 3D by repeating experiments in multiple planes [6]; however, measurement techniques for instantaneous quantification of a 3D volume are still a developing research area. A variety of different techniques have been and are still currently being developed to fill this void. These techniques range from the use of multiple cameras to scanning techniques.

Stereo imaging uses two cameras viewing the same region of space capturing images at the same time to obtain the out of plane velocity component of the fluid motion, resulting in three component velocity vectors. To make truly 3D velocity measurements a larger number of cameras must be used, as in tomography which generally uses four cameras viewing the region of interest simultaneously. Though tomography has been shown to produce highly accurate 3D velocity measurements, this technique faces limitations in some experimental configurations. Not only does the use of four cameras require careful calibration in camera placement, but there are also many experimental configurations which allow only limited optical access, such as wind tunnels with only one viewing port. In these situations it is impractical and often impossible to view the region of interest from four different angles [5].

Two currently developing techniques for instantaneous measurement of 3D particle fields which require only a single camera are plenoptic imaging and digital in-line holography (DIH). Plenoptic imaging is an implementation of light field imaging which uses a camera modified by the insertion of an array of microlenses between the main lens and the image sensor to collect both the spatial and angular information of the incoming light rays. This information is encoded in the recorded image and can be computationally restructured in post processing to produce a 3D representation of the particle locations and sizes [7]. DIH is a specific implementation of holography, which is a laser based technique in which the particle field of interest is illuminated by a laser and the diffraction pattern created by the interaction between the particles and the laser volume is recorded on a digital image sensor. These diffraction patterns can then be computationally manipulated in post processing to create a 3D representation of the volume similar to that of plenoptic imaging. DIH uses a digital image sensor rather than a traditional holographic film plate and a single laser beam rather than separate illumination and reconstruction beams [8]. Both of these elements reduce the experimental complexity of the system and improve the accuracy of the reconstruction.

Though the methodologies of these two techniques are significantly different, they are both designed with similar concepts in mind, as demonstrated not only by the resulting data, but also by examination of the words *holography* and *plenoptic*. First consider that the word *photography* is derived from the Greek words *photo* meaning light and *graphein* meaning to write. Similarly, *holography* is derived from the Greek words *holos* meaning whole, entire, or complete, and again *graphein. Plenoptic* at first glance does not appear similar, but it is in fact derived from *plenus* meaning complete or full and *optic* meaning visible or seen. Examination of these root words shows a clear analogy between the two techniques as they are both intended to view and record a

complete visible scene [9], [10]. Here, these two techniques are compared in order to reveal the strengths and weaknesses of each.

In this work this comparison is made by repeating two particle tracking experiments with plenoptic imaging which have been previously executed using DIH. Then the results of all four experiments are analyzed to determine the specific differences between the two techniques in terms of experimental complexity, data processing capabilities and requirements, and accuracy of particle location.

Chapter II gives an overview of light field imaging in general and specifically the developments of the plenoptic camera as a diagnostic tool over the last twenty five years. This chapter also includes a discussion of the structure of the light field data captured using a plenoptic camera and the computational algorithms used to manipulate this data to provide 3D information about a scene. Chapter III similarly provides an overview of the development of holography since its origins in the late 1940's and the various configurations in which it has been applied as well as a brief introduction to the mathematics behind holographic reconstruction. Additionally, this chapter describes DIH and reviews the results of the two experiments previously executed. Chapter IV describes the two experiments examined in this work. First, the drop impact experiment is examined in which a drop of water is released onto a thin film of water and two images of the resulting field of secondary droplets are captured in quick succession. Multiple runs of this experiment were executed in which the initial height from which the drop is released as well as the time after impact that the images are captured is varied. These variations provide data sets in which the secondary droplet field is in different stages of development. In the second experiment a shotgun is fired and two images of the shotgun pellet field are captured. Chapter V describes the data processing methods used to determine the particle locations and sizes from the DIH and

plenoptic volumes as well as the challenges encountered and improvements made to these algorithms during this work. Also in this chapter is a description of the particle tracking algorithm used to match particles between the two frames to determine 3D velocities. Chapter VI discusses the results of each experiment and demonstrates trends which appear in the data based on a variety of parameters. This includes discussion of both qualitative and quantitative aspects of the results. Finally, Chapter VII summarizes the findings of these previous chapters and draws conclusions in the overall comparison of DIH and plenoptic imaging.

II. Light Field Imaging

A. The Light Field Concept

The concept that light flows through space dates back to the 15th century and Leonardo da Vinci's assertion that an infinite number of light rays move in all directions from all objects. He also surmised that by viewing a scene through a pinhole camera one is viewing the projection of a cone of these light rays, which he termed a 'visual pyramid' [11]. Light was first interpreted as a field by Michael Faraday in 1846, a proposal he based on analogies to his work in magnetism. This was later formalized by James Clerk Maxwell's famous equations [12].

In 1936 Arun Gershun first proposed application of these mathematical concepts to the measurement of light and defined the light field as the amount of light traveling in every direction through every point in space. However, he could not actually make light field measurements prior to the invention of the digital computer [12]. Rapid advancement in the field of light field imaging began in the early 1990's with the mathematical definition of the plenoptic function by Adelson and Bergen who aimed to characterize all basic visual measurements with a single multidimensional function. This plenoptic function was developed to measure every view, at every moment, from every location, at every wavelength. This results in a 7D function of the form shown in Equation (1).

$$P = P(\theta, \phi, \lambda, t, x, y, z) \tag{1}$$

In this equation (x, y, z) are all the possible locations, (θ, ϕ) are all the possible angles of ray propagation, λ represents all possible wavelengths, and t represents all possible times [10]. In application to photography this function is simplified to a 5D function because the photo represents

only a single time and it is assumed that the wavelength of a particular light ray is unchanging. This can be further reduced to a 4D function under the assumption that the light field is in a transparent medium and the propagation along one of the spatial coordinates is a straight line. This 4D light field defines the radiance along rays in empty space. For convenience, a two plane parameterization can be used to define the light field, which uses four spatial coordinates. The light field is then denoted $L_F(s,t,u,v)$ where the light ray intersects one plane at (u,v) and the other at (s,t) thus fully defining the location of the ray [12]. A schematic depiction of this two plane parameterization is shown in Figure 1 below.

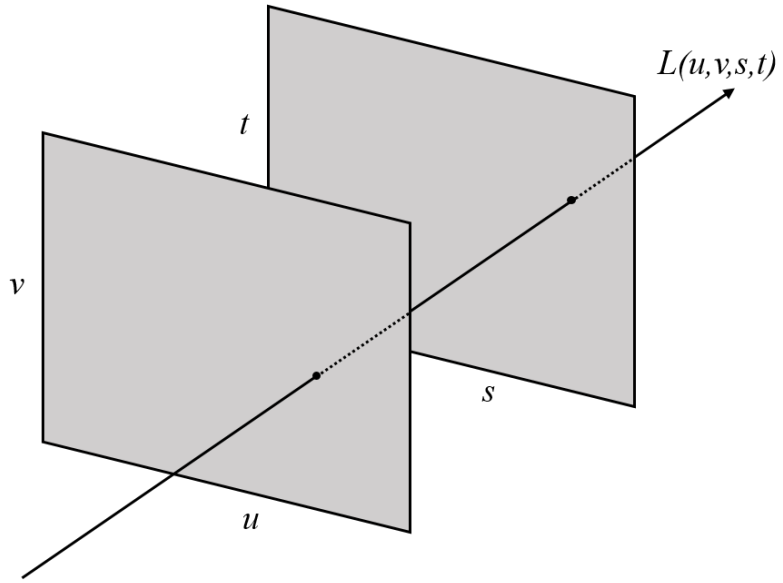

Figure 1: Two plane parameterization of the light field

B. The Plenoptic Camera

Plenoptic imaging is an emerging technology, which allows for instantaneous 3D imaging of a scene using a single camera and white light illumination [13]–[15]. A conventional camera maps a 3D scene in object space to a 2D image plane such that the angular information of the incoming light is lost. In contrast, a plenoptic camera includes a custom microlens array between the main lens and image sensor to record the entire 4D light field described above [12].

1. Origins and Development

The first implementation of a plenoptic camera was executed by Adelson and Wang in 1992 to achieve what was termed single lens stereo. The driving concept behind single lens stereo is that over the large aperture of a conventional camera, the light striking different regions actually provides different information specific to the view from that location. A traditional image is simply the average of all these different perspective views. Therefore, by discretizing the main lens in some way, these different views can be sorted out and recreated; this discretization is achieved by the microlens array. The optical configuration employed by Adelson and Wang was more complicated than current plenoptic cameras. It consisted of a main lens outfitted with a weak diffuser, a field lens which places the main lens at optical infinity from the microlens array, the microlens array itself, a relay lens for improved flexibility, and finally the image sensor. A fine ground glass diffuser is also included to improve problems which were encountered with vignetting [11].

A more compact version of the plenoptic camera was created by Ng *et al* in 2005. This plenoptic camera was based on only a main lens, microlens array, and image sensor and was constructed using a medium format digital camera modified by the insertion of a microlens array. A simple schematic of these components is shown in Figure 2. In this figure the discretization of the light rays based on angle of propagation is represented by displaying the segment of rays reaching each image sensor pixel with a different color. This design resulted in a hand held plenoptic camera, which was operated no differently than a consumer digital camera [13].

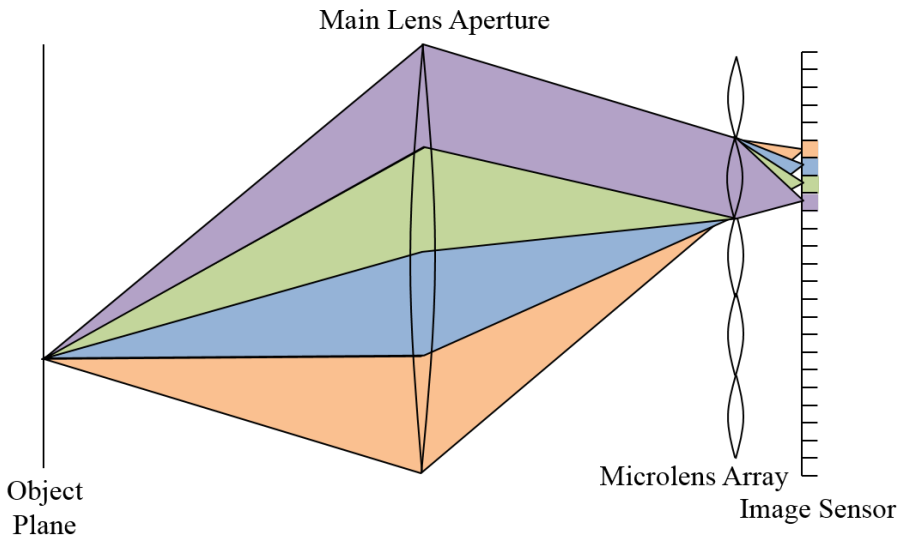

Figure 2: Schematic of the main components of a plenoptic camera

2. Current Implementation

The plenoptic camera used in this work was constructed by the Advanced Flow Diagnostics Laboratory (AFDL) at Auburn University using an Imperx Bobcat B6640 29 MP camera, which has a CoaXPress KAI-29050 CCD image sensor (6600 × 4400 pixels, 5.5 µm pixel pitch). The maximum frame rate is 20 frames per second and tiff images are recorded. The camera is modified by the addition of a microlens array with 471 × 362 hexagonally arranged microlenses positioned approximately 308 µm from the image sensor using a custom mount designed by the AFDL. This mount, with the microlens array in place, is shown in Figure 3.

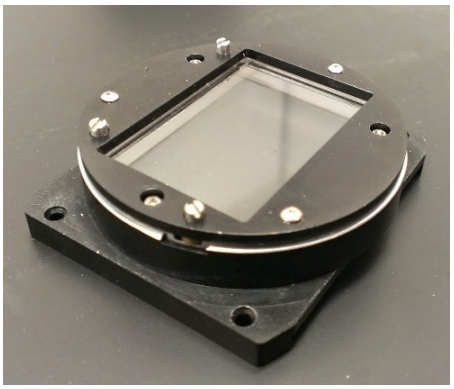

Figure 3: Custom designed mount and microlens array

The hexagonal arrangement allows the microlenses to be packed closer together for more efficient use of the available image sensor surface area than a rectangular arrangement of microlenses. The pitch of the microlenses is 77 μm. After plenoptic processing the resolution of the output images is approximately 900 × 600 pixels. Figure 4 is a photo of this camera, shown with a 60 mm Tamron main lens.

Figure 4: Plenoptic camera currently in use at Auburn University equipped with a 60 mm Tamron main lens

3. Development of the Light Field Equation

Each microlens creates a sub image of the light field in the aperture of the main lens, thereby encoding information on the angular distribution of light rays in the aperture plane. With appropriate calibration, each pixel in the sensor plane can be assigned a spatial position based on the center of the microlenses and an angle of propagation based on the location of the pixel within each sub-image [12].

This information can be decoded using the two plane parameterization. Each microlens has a number of image sensor pixels behind it, which results in a raw image consisting of many sub aperture images each formed by the view of the aperture from an individual microlens. The center

of each sub aperture image is assigned (s, t) coordinates based on the location of the corresponding microlens, while each pixel within the sub image is assigned (u, v) coordinates based on the corresponding location on the main lens aperture [12]. A raw plenoptic image is shown in Figure 5. In visual examination of this image, it appears quite similar to a standard photograph except for faint lines which appear to be aliasing. These lines are a result of the rows of sub aperture images of each microlens, which are clearly shown in the inset of this figure.

Figure 5: Raw plenoptic image

The decoding of these sub aperture images and thus synthetic image formation is based on the relationship between the light field *L* and the synthetic light field *L'*. This relationship is defined by the distances between the physical main lens aperture plane and the microlens plane

(shown in Figure 2) and the virtual aperture plane and virtual image sensor plane all shown in Figure 6 [13].

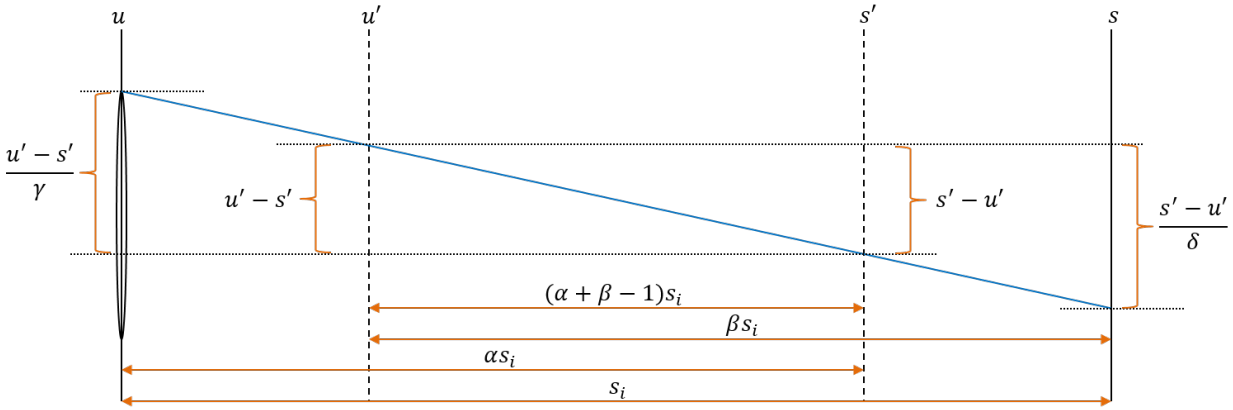

Figure 6: Synthetic light field relationships

The virtual planes are the planes where these components would have been for a given synthetic image. In this schematic *u* denotes the main lens aperture plane, *u'* denotes the virtual aperture plane, *s* denotes the microlens plane, and *s'* denotes the virtual image sensor. The relative locations of these planes are determined based on the parameters α and β, which determine where the virtual aperture and virtual image sensor are located respectively. Also, in this schematic, γ and δ are defined by Equations (2) and (3) respectively.

$$\gamma = \frac{\alpha + \beta - 1}{\alpha} \tag{2}$$

$$\delta = \frac{\alpha + \beta - 1}{\beta} \tag{3}$$

The real physical distance between the main lens aperture and the microlens array is the image distance s_i, which can be determined from the thin lens equation based on the focal length of the main lens and the nominal magnification of the scene as in Equation (4).

$$s_i = f(1 - M) \tag{4}$$

The relationship between the light field L and the synthetic light field L' is formalized by Equation (5) as derived by Ng et al [13]. Note that in this equation v and t are the directions perpendicular to u and s respectively as shown previously in Figure 1.

$$L'(u', v', s', t') = L\left(s' + \frac{u' - s'}{\gamma}, t' + \frac{v' - t'}{\gamma}, u' + \frac{s' - u'}{\delta}, v' + \frac{t' - v'}{\delta}\right) \quad (5)$$

This leads to the synthetic photography equation, derived by Ng *et al* [13], shown here in Equation (6) where A defines whether a given location is within the aperture and E is the image that would have appeared on the virtual image plane.

$$E(s', t') = \iint L'(u', v', s', t')\, A(u', v') du dv \quad (6)$$

Finally, the plenoptic function can be used to recreate images of a given scene at different angular perspectives or numerically refocused along the optical depth [13]. For example, Figure 7 shows a plenoptic recording of the splash from the impact of a water drop on a thin film of water and images, which have been numerically refocused along the optical depth.

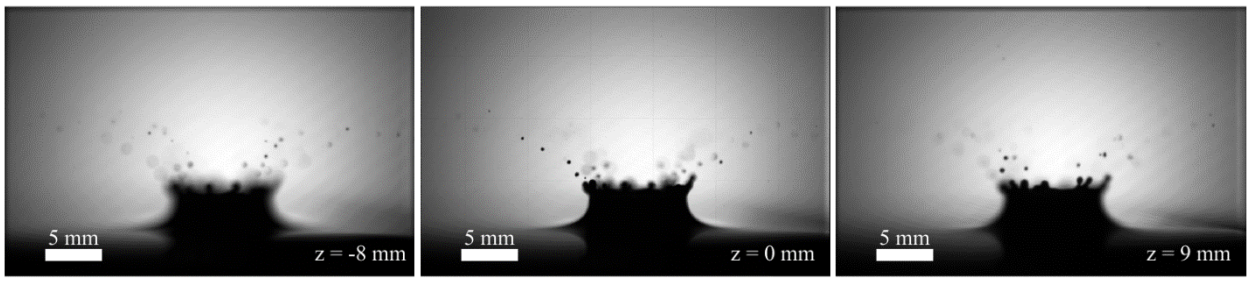

Figure 7: A single raw plenoptic image of a drop impact refocused to three different planes

4. Perspective Shift

From a single raw plenoptic image, views from a variety of perspectives can be created by varying the location behind each microlens from which the image data is drawn. As shown in Figure 8, a perspective image is made up of a single pixel from behind each microlens. Selecting pixels from the same location relative to each microlens produces a synthetic image as if the scene

was viewed from a camera with a much smaller aperture, analogous to a pinhole camera, at the corresponding location on the main lens. This location on the main lens is defined by (u, v) coordinates as described previously. It should be noted that this is a simplified explanation of the computational method used to create perspective shifted images. In reality, the image sensor pixels are not perfectly aligned with the microlens array as shown here, there is generally some rotation and offset between the two grids. Additionally in the current implementation, the microlenses are arranged in a hexagonal rather than rectangular pattern. Therefore, a 4D interpolation is carried out to determine the pixels intensities of interest for creation of the output image.

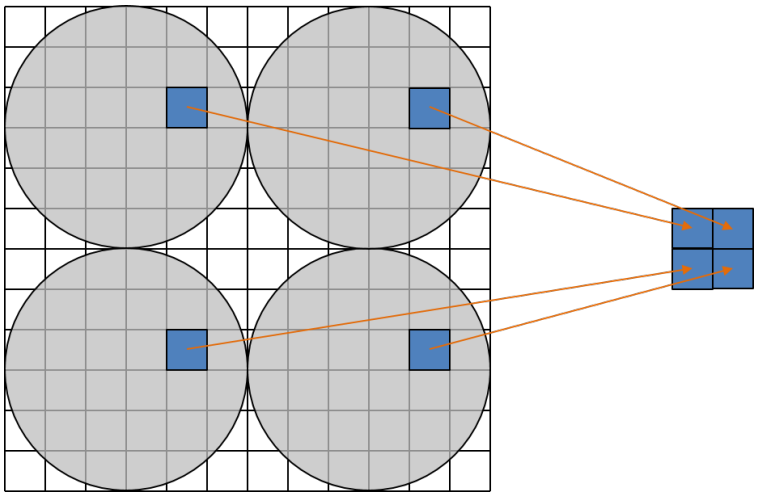

Figure 8: Perspective view creation

These synthetic perspective images have a very large depth of field because of the small subset of the main lens aperture from which they are formed, resulting in an image similar to that captured using a pinhole camera. The depth of field of a perspective image can be approximated using Eq. (7).

$$DOF = \frac{s_o f^2}{f^2 - \frac{f}{d} c(s_o - f)} - \frac{s_o f^2}{f^2 + \frac{f}{d} c(s_o - f)} \tag{7}$$

In this equation the value of *d* is representative of the effective size of the aperture. In perspective shift images this is equivalent to the diameter of the main lens aperture divided by the image sensor

pixel pitch, which is equal to 14 in the camera used in this work. Therefore, the depth of field of a perspective shifted image is approximately 14 times larger than the depth of field of a refocused image, which uses the entire aperture. Examples of these perspective shifted images are shown in Figure 9. The large depth of field is evident in noting that nearly everything in this image is in focus, from the people at the back of the room to the boxes in the foreground. The change in the perspective from which the scene is viewed is particularly evident in comparing the distances between objects in the two views as shown in the locations circled in red.

Figure 9: Example perspective views

The creation of a perspective view can be defined by a simplification of the synthetic photography equation shown in Equation (8). In this equation (u_0, v_0) is the location of the perspective view images on the main lens plane and $\alpha = 1$ for simplicity because the location of the focal plane is not relevant to the result [13].

$$E(s', t') = L'\left(s' + \frac{u_0 - s'}{\beta}, t' + \frac{v_0 - t'}{\beta}, s', t'\right) \tag{8}$$

5. Computational Refocusing

Additionally, and of particular interest in this work, a raw plenoptic image can be used to create images refocused to different depths both in front of and behind the nominal focal plane. An example of this refocusing capability is shown in Figure 10 below. In comparing these two

images it is obvious that in the image on the left the people and objects near the back of the room are in focus while the words on the box in the foreground are unreadable. In the image on the right the box in the foreground is in focus and the faces in the background are undistinguishable.

Figure 10: Example refocused images

The concept of creating a refocused image is shown schematically in Figure 11. Light rays emanating from a point on the nominal focal plane, shown in orange, focus to a single point on the microlens array, therefore, objects at that depth will appear in focus. The nominal focal plane is a distance s_o from the aperture plane and the microlens plane is a distance s_i from the aperture plane. The concept of refocusing of course is to move the focal plane to another depth, known as the refocused plane, which corresponds to a virtual image sensor plane. The refocused plane is a distance s_o' from the aperture plane. The virtual image sensor plane is the plane where the rays from this distance would have been focused. The virtual image sensor plane is a distance s_i' from the aperture plane and is defined as $\alpha \cdot s_i$. Therefore, when α is larger than 1 the resulting image is focused closer to the camera than the nominal focal plane and when α is smaller than 1 the resulting image is focused farther from the camera than the nominal focal plane [13].

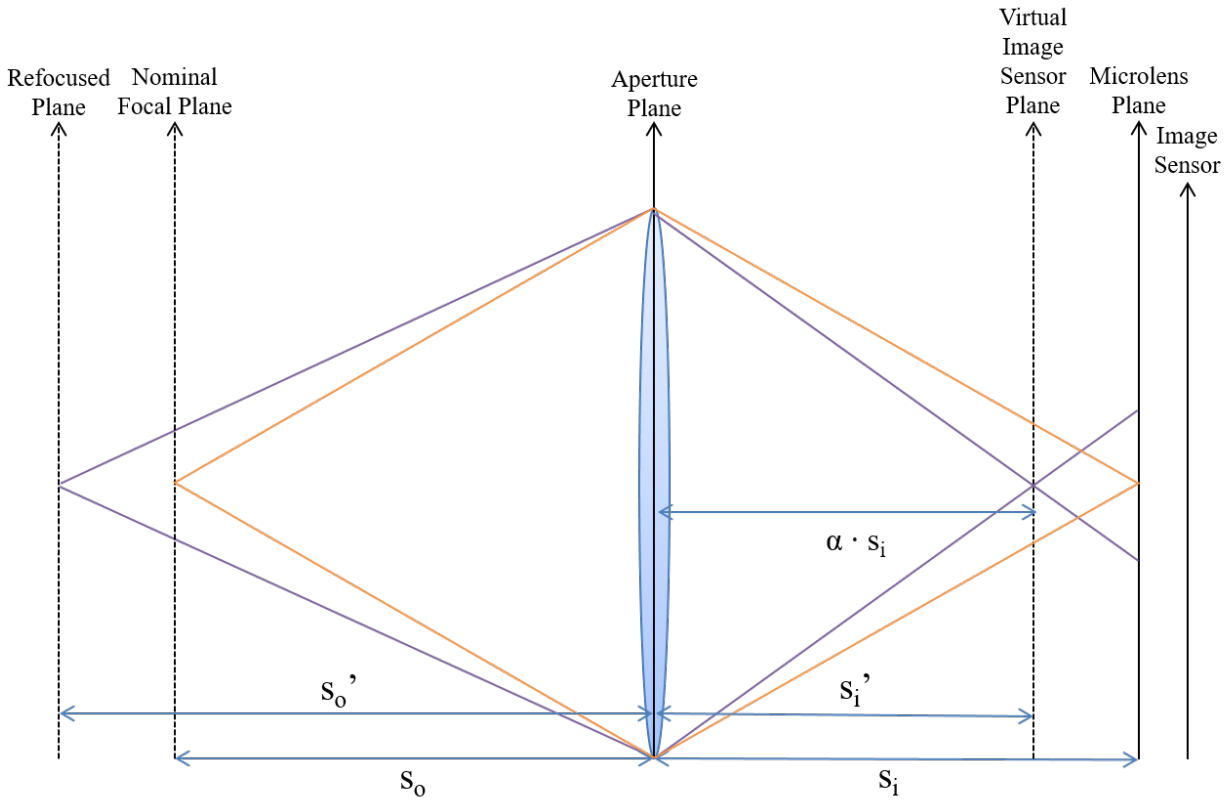

Figure 11: Refocused image schematic

The creation of a refocused image can also be represented by a modified version of the synthetic photography equation as in Eq. (9).

$$E(s',t') = \iint L'\left(u',v',u' + \frac{s'-u'}{\alpha}, v' + \frac{t'-v'}{\alpha}\right) du'dv' \qquad (9)$$

In this equation α defines the location of the virtual image sensor plane and corresponds to the depth to which the scene is computationally refocused. Additionally in refocusing, the virtual aperture plane does not move therefore, $\beta = 1$. A full aperture is used so, $A(u',v') = 1$. This equation can be simply described as a summation of shifted versions of the pinhole images used to create the perspective shifted images described in the previous section [13].

Physical coordinates can be derived from the value of α using the thin lens equation, the focal length of the main lens, and the magnification at the nominal focal plane. The magnification,

M, is defined as the ratio of the image distance to the object distance. From the schematic in Figure 11 it is also apparent that $\alpha = s_i'/s_i$. Rearranging the thin lens equation and substituting in the magnification relationship results in Equation (10), where f is the focal length of the main lens.

$$s_i = (1 - M)f \tag{10}$$

This equation is used to find s_i, then s_o is determined using the magnification relationship. Then, s_o' is defined relative to s_o. For instance, if $s_o' = s_o + z$, then the refocused plane is located a distance z farther from the camera than the nominal focal plane. The thin lens equation in combination with the α ratio can then be used to relate α and z as in Eq. (11).

$$\alpha = \frac{1}{\left(\frac{1}{f} - \frac{1}{s_o + z}\right) s_i} \tag{11}$$

One of the most significant benefits of the plenoptic camera examined by Ng *et al* is the improvement in signal to noise ratio achieved by refocusing as compared to conventional imaging with an equivalent depth of field. This improvement is due to the large aperture used in plenoptic imaging [13].

6. The Light Field Imaging Toolkit

The Light Field Imaging Toolkit (LFIT) is a collection of MATLAB® functions developed by the Advanced Flow Diagnostics Laboratory (AFDL) at Auburn University to process light field images. LFIT's functionality is focused on creating perspective and refocused images with a high level of flexibility. LFIT includes a graphical user interface (GUI) system, shown in Figure 12, to allow the processing of light field data without extensive MATLAB® knowledge on the part of the user, but also includes a batch mode option to allow the interested user to not only process large amounts of data but also to create customized scripts based on specific computational needs.

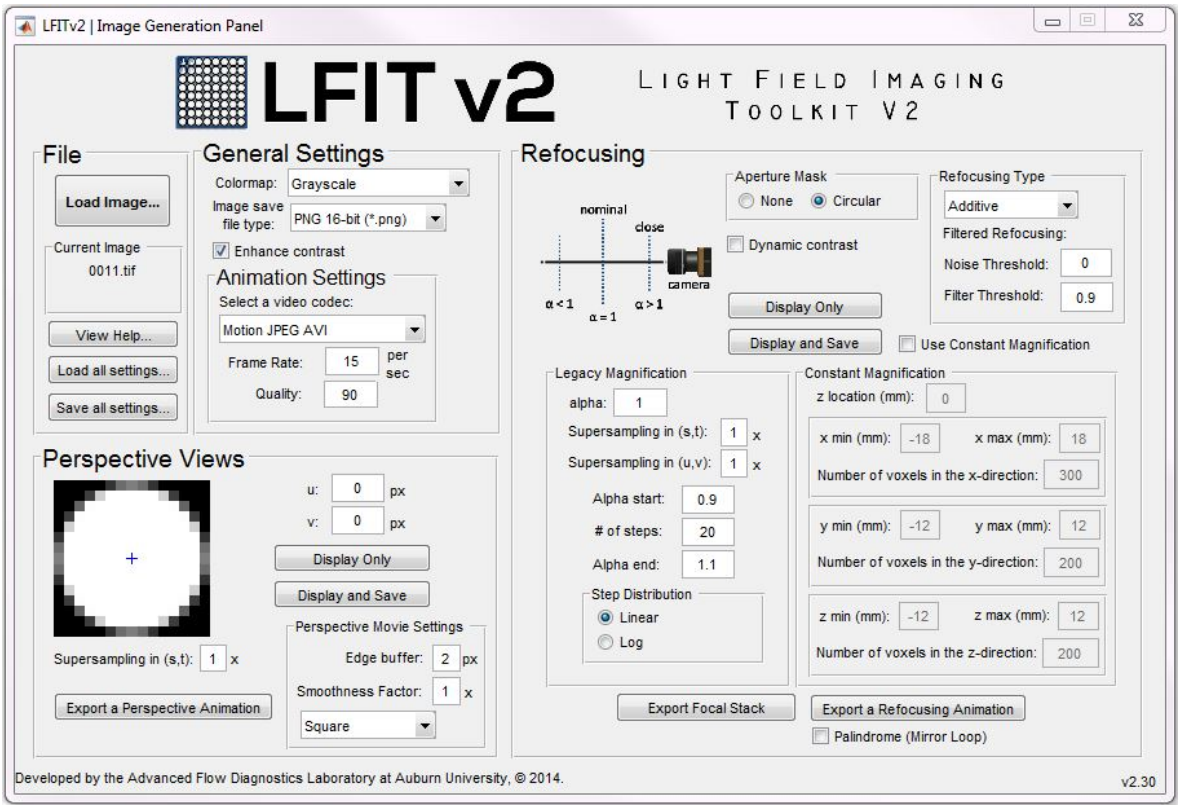

Figure 12: LFIT GUI

The existing functions can also be modified by the user as LFIT is an open source software package available at https://github.com/AFDL. In addition to the creation of single perspective and refocused views, the user can choose to create entire focal stacks, or refocused and perspective shifted movies.

7. Advantages and Limitations

One of the most striking benefits of plenoptic imaging is the compact size of the camera as well as the fact that dense angular information can be collected in a single snapshot using a single camera. These physical attributes provide critical advantages in applications where imaging of regions with limited optical access is required. Additionally, plenoptic imaging does not require the use of a coherent illumination source, which simplifies the required experimental setup and in some scenarios can remove unwanted image processing artifacts.

The most significant limitation that plenoptic imaging currently faces is the limited resolution of the resulting images. The resolution of processed plenoptic images is limited by the number of microlenses as spatial resolution is traded for the angular resolution achieved by the multiple image sensor pixels behind each microlens. In the camera used in this work, each the diameter of each microlens is 14 times the diameter of an image sensor pixel, therefore, there are approximately 196 image sensor pixels behind each microlens all of which contribute to a single pixel in processed plenoptic images. Supersampling during data processing and resampling the hexagonal microlens grid onto a rectangular image grid achieves approximately 4 output image pixels per microlens, however, there this does not necessarily correspond to improved resolution. As digital image sensor technology improves and higher resolution image sensors are available, this limitation is expected to become less significant.

III. Holography

Holography is a method of recording and reconstructing light waves diffracted by an object which is illuminated by coherent light. The diffracted wave is known as the object wave and interferes with a reference wave. Since the waves are coherent, an interference pattern is created which contains information about the phase and amplitude of the diffracted wave from which they can be reconstructed. This is in contrast to photography, which does not record phase information. This interference pattern is known as the hologram and is recorded as intensity variation on holographic film or a digital image sensor [16], [17].

Conventional imaging techniques produce a 2D picture of a 3D scene by recording the intensity distribution of the scene on a light sensitive surface. These techniques do not capture phase information about the incoming light waves. In contrast, a hologram is recorded on a 2D surface but produces a 3D image. This is accomplished by recording both the phase and amplitude of the incoming light waves. The difficulty in holographic recording is that recording mediums such as film and digital image sensors are only sensitive to intensity, therefore, the phase must somehow be converted into intensity variations to be recorded [18]. This is accomplished by illuminating the subject with coherent light and recording the diffracted waves. The relative wave between the photographic subject and the reference wave can then be measured as a change in intensity. The hologram can then be re-illuminated with the reference wave (either optically or digitally) to reconstruct the scene. The use of holography is not limited to visible light waves but can also be implemented using any other waves such as x-rays or even acoustic waves [16]. Holography is generally implemented as a lens-less imaging system when used to reconstruct

particle fields. This results in the aperture being limited only by the area on the holographic plate or digital image sensor that sees the light scattered by the particle field. This eliminates issues associated with large optics, such as excessive aberrations, and allows for a larger recording area in general [19].

A. Origins

Holography was invented in 1949 by Dennis Gabor who proposed adding a coherent reference wave to the object wave and recording the interference pattern on film. The film could then be developed and illuminated to reproduce the complex amplitude of the light waves. At the time of his invention, however, a coherent light source was not available, which hindered the development of the technique. The development of the laser in the early 1960's filled this void and began the rapid development of holography, which continues to the present day [17], [20].

1. Mathematical Model

The mathematical models used to describe holograms vary greatly depending on the particular recording scheme used and application for which the system is intended. The interference, I_h, between the complex reference wave, R, and the object wave, O, can be described by Eq. (12).

$$I_h(x_h, y_h) = (R + O)(R^* + O^*) = RR^* + RO^* + R^*O + OO^* \tag{12}$$

where '*' denotes the complex conjugate and (x_h,y_h) is a point on the hologram. The reconstruction of the incident light illuminating the object, U_r, created by illuminating the hologram with a conjugate reference wave, is represented by Eq. (13).

$$U_r = R^* I_h = \|R\|^2 R^* + \|R\|^2 O^* + R^{*2} O + R^* O O^* \tag{13}$$

The first term represents the reference wave, the second is the reconstructed object wave, and the third is the virtual image [2].

2. Types of Holography

There are several major types of holography. Fresnel holography was introduced by Gabor and involves recording the interference pattern between the object diffraction wave and reference wave. The hologram is then illuminated by a replica of the reference wave. The quality of the reconstruction is based on the angle between the reference wave and the diffraction wave. Fraunhofer holography is an in-line system where the object is transparent enough to allow un-diffracted light to provide the background. The hologram is recorded in the far-field of the object. Fourier holography is used for reconstruction of 2D objects and is recorded with the planar object and the reference source in the same plane [21].

3. Depth of Focus Problem

One significant limitation in holography, which became apparent in the early work in holography, is the depth-of-focus problem. Due to the limited angular aperture of the holographic system, the depth-of-focus is relatively large, which limits the resolution in the depth direction (along the optical axis). The depth of focus of the reconstructed images depends on the angular aperture of the hologram, the angular aperture being the apparent angle of the lens as viewed from the focal point. The effective angular aperture, the angular range over which the laser light contributes to imaging, is defined by Eq. (14) where λ is the wavelength of the illuminating light and d is the diameter of the particle.

$$\Omega = \lambda/d \tag{14}$$

Based on examination of a point source in a diffraction limited system it has been determined that the depth of focus for a point source is approximately equal to λ/Ω^2, which is equivalent to d^2/λ by substitution of Eq. (14). The depth of focus is equivalent to the resolution

in the depth (longitudinal) direction as shown in Eq. (15). Equation (16) shows the resolution in the plane perpendicular to the optical axis.

$$x_l \approx \lambda/\Omega^2 \tag{15}$$

$$x_t \approx \lambda/\Omega \tag{16}$$

These equations show that the resolution is worse in the longitudinal (depth) direction and that the angular range should be as large as possible to increase position resolution. This means that systems should be designed so that the objects being imaged are as close to the hologram as possible to increase this angle [8], [19].

Numerous highly varied efforts have been made to improve the depth resolution in holography. One method illuminates the particle field with one or more parallel light sheets and records a single hologram, which allows precise determination of the axial position of the particles but not of the axial velocity. The use of off-axis holography, described in section III.B.1 below, with a large angle between the object and reference beams, has been used successfully to improve resolution, because increasing the angle reduces the depth of focus. Recording multiple holograms simultaneously from different directions can also improve the resolution but adds logistical complexity to the system [2].

B. Experimental Configurations

Holography has been implemented using a wide variety of experimental setups. Most of these methods can be classified as either off-axis or in-line holography. The main difference in these two methods is that off-axis holography uses separate reference and object beams while in-line holography uses a single beam. Figure 13 and Figure 14 display holographic recording and reconstruction using off-axis and in-line configurations. Casual examination of these schematics shows that off-axis requires a more complicated experimental setup, however, there are several

other significant differences between the implementation and data processing of the two configurations [22].

1. Off-Axis Holography

Figure 13 (left) is a schematic of off-axis recording. The illuminating beam (or object beam) is directed through the particle field and light scattered by the particles is incident on the recording medium. The reference beam is directed undisturbed at a known angle towards the recording medium and the interference pattern is therefore formed by the combination of the scattered object light and the reference beam. Figure 13 (right) shows the reconstruction of off-axis holography. The hologram is illuminated with a conjugate reference beam, which is simply a beam at the same angle as the original reference beam but propagated in the opposite direction, and 3D virtual and real images of the particle field are formed as shown in Figure 13 (right). This configuration reduces speckle noise because there is not interference between two waves within the particle field. Off-axis holography usually requires high laser energy because it does not use forward scattered light, therefore more laser energy is required to produce a substantial signal. Off-axis HPIV requires a complex optical system and is generally used in situations which require low speckle noise [2].

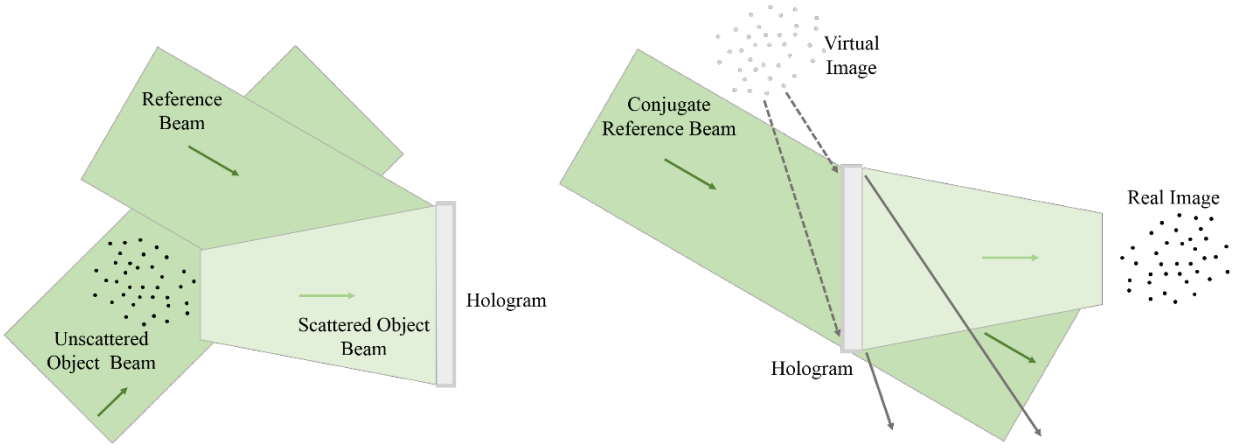

Figure 13: Off-axis recording (left), off-axis reconstruction (right)

2. In-Line Holography

Figure 14 (left) displays in-line recording, which consists of a single beam directed through the particle field toward the recording medium. The light which is scattered by the particles becomes the object beam and the undisturbed part of the beam becomes the reference wave. The reconstruction is then created, as in Figure 14 (right), by illumination of the hologram with a conjugate reference beam which produces 3D virtual and real images of the particle field [23]. Although the use of a single light beam greatly simplifies the execution of this technique there are drawbacks in the use of this configuration. Speckle noise in the reconstructed image as a result of interference between the scattered waves is prominent in in-line holography and significantly degrades the quality of the reconstruction. High particle density can reduce the coherence of the remaining reference beam. This limits the density of particles and the volume depth which can be accurately reconstructed. Some attempts have been made to improve image quality by removing un-diffracted light with a high-pass filter, however, the improvements of this removal are minimal as compared to the results of an off-axis system. The establishment of digital holography has also allowed for improvements in the technique [24], [25].

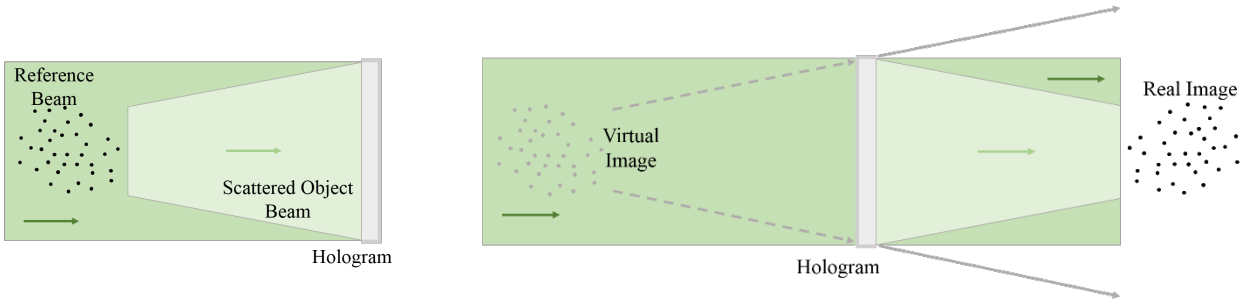

Figure 14: In-line recording (left), in-line reconstruction (right)

C. Recording Mediums

Traditional holography uses film recording and optical reconstruction producing high resolution results but, requires logistically taxing chemical processing. As digital image sensors

have developed, digital holography, using digital recording and numerical reconstruction, has grown increasingly popular as well. A variety of factors impact the selection of the recording medium used in holography.

The numerical reconstruction can be computed using Rayleigh-Sommerfield diffraction theory as in Equation (17).

$$U(x,y,z) = \frac{1}{j\lambda}\iint H(\xi,\eta)R(\xi,\eta)\frac{\exp(jk\rho)}{\rho}cos\Theta d\xi d\eta \tag{17}$$

In this equation, $H(\xi,\eta)$ is the intensity in the hologram plane, $R(\xi,\eta)$ is the reference wave, ρ is the distance from the point (x,y,z) in the reconstruction to the point $(\xi,\eta,0)$ in the hologram plane, λ is the wavelength of the light, and $cos\Theta$ is the obliquity factor, which can usually be set to 1. This equation can be interpreted as the convolution of $H(\xi,\eta)R(\xi,\eta)$ and the diffraction kernel $g(x,y)$, defined in Equation (18). Therefore Equation (17) can be computed using FFTs for each plane [8].

$$g(x,y) = \frac{1}{j\lambda}\frac{\exp(jk\sqrt{x^2+y^2+z^2})}{\sqrt{x^2+y^2+z^2}} \tag{18}$$

1. Film Holography

Film recording generally uses silver halide holographic film. Specialized fine grain emulsions have been developed to resolve the interference pattern in microscopic detail, generally on the order of a wavelength. This allows for storage of a huge amount of information in the case of a 12x9 cm^2 photographic plate with a resolution of 5000 lines/mm, which is a fairly standard holographic film size [19]. This medium provides a high resolution hologram, however, the availability of digital sensors makes digitizing an attractive choice to avoid the necessary chemical processing. Despite the inconvenience of chemical processing, film holography remains a popular experimental choice because digital image sensors cannot yet provide the resolution of holographic film [8].

2. Digital Holography

The use of holography systems with digital image sensors is an increasingly popular technique because digital holography not only removes the necessity of chemical processing but also replaces optical reconstruction with numerical reconstruction algorithms. Although there are resolution limitations in the use of digital image sensors, there are a wide range of benefits from using a digital system for holography other than simply the logistical simplifications. Digital holograms can be preprocessed before reconstruction to remove noise and correct aberrations that result from imperfections in the experimental conditions. These capabilities make it unnecessary to use an off-axis configuration because the issues with in-line recording can be corrected or removed. Additionally, difficulties arise in the use of an off-axis configuration with low spatial resolution digital image sensors because of high spatial frequency fringes, which cannot be resolved [8].

D. Digital In-Line Holography

Digital in-line holography (DIH) is a laser based technique for 3D measurement of a particle field. As illustrated in Figure 15, DIH is again a two-step process comprised of recording and reconstruction. Recording is accomplished by illuminating a particle field with a collimated laser beam and recording the resulting diffraction patterns on a digital image sensor. The interference of a conjugate reference wave with the recorded hologram allows for an estimate of the phase and amplitude of the light at the recording plane [26]. By solving the diffraction integral equation, this complex amplitude is numerically refocused to any optical depth, z, revealing images of particles at their original locations. With appropriately defined processing routines, 3D particle positions and sizes can be automatically measured from recorded holograms.

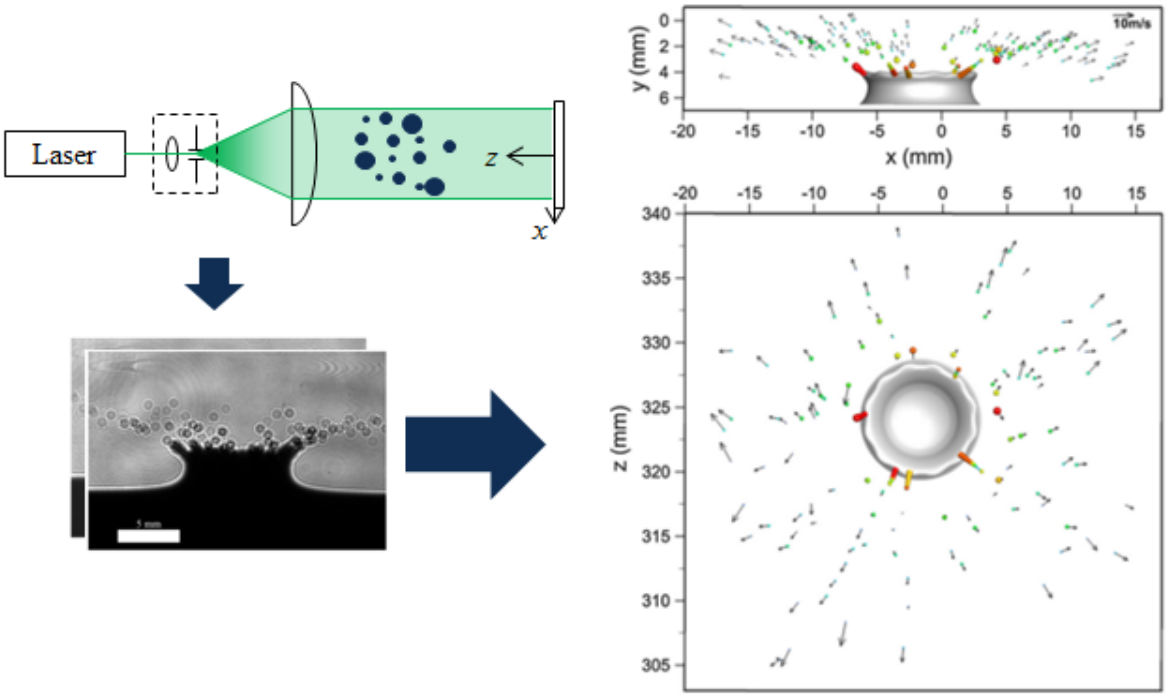

Figure 15: Digital in-line holography

1. Applications to Particle Tracking

In Guildenbecher *et al* 2014 [27] DIH was applied to measure the 3D motion of secondary fragments which form from the impact of a water drop on a thin film of water. Figure 15 shows example holograms and the reconstructed 3D particle field. In a second example, Guildenbecher *et al* 2014 [4] applied DIH to study the 3D motion of pellets from a shotgun traveling near sonic conditions. As is discussed in more detail in subsequent sections, these two highly varied experiments illustrate a number of the strengths and weaknesses of the DIH technique. Therefore, by executing these same experiments using plenoptic imaging a reasonable comparision of the two techniques can be made.

2. Advantages and Limitations

Holography provides a wide variety of benefits. Among the most notable, the measurements are noninvasive, objects of interest can be arbitrarily shaped, deformation of

different states of matter can be measured, and high resolution and accuracy can be achieved [9]. One limitation encountered in holographic imaging is the limited field of view which can be achieved using reasonably sized optics. Additionally, the requirement that a coherent illumination source is used can create problems in imaging high speed compressible flows, as shock waves can cause unwanted artifacts in the reconstructions.

IV. Experiments

The two experiments using plenoptic imaging examined in this work are modeled after those previously conducted using DIH to allow for direct comparison of the two methods. The first is a drop impact experiment in which the motion of a secondary droplet field is examined. The second experiment examines the motion of shotgun pellets travelling at near sonic conditions. Both experiments were conducted at Sandia National Laboratories at Kirtland Air Force Base in Albuquerque, New Mexico. Though these two experiments use relatively similar configurations, they allow for the study of two very different flow fields. The drop impact experiment applies these techniques to a low speed flow with small, non-uniformly sized particles. The shotgun experiment examines a high speed compressible flow and larger uniformly sized spherical particles.

A. Drop Impact Secondary Droplet Tracking

Plenoptic imaging is applied to quantify the motion, size, and shape of secondary fragments produced by the impact of a water drop on a thin film of water. As was done in Guildenbecher *et al.* 2014 [27], a syringe pump filled with deionized water produced droplets which left a syringe tip at approximately zero velocity and were accelerated by gravity to impact a thin film of deionized water contained in a rubber o-ring affixed to a smooth acrylic surface. The thickness of the film was equal to the height of the o-ring (2.35 mm) and the relatively large diameter of the o-ring (50.8 mm) prevented interaction of the breakup process with the edges. A schematic of this configuration is shown in Figure 16.

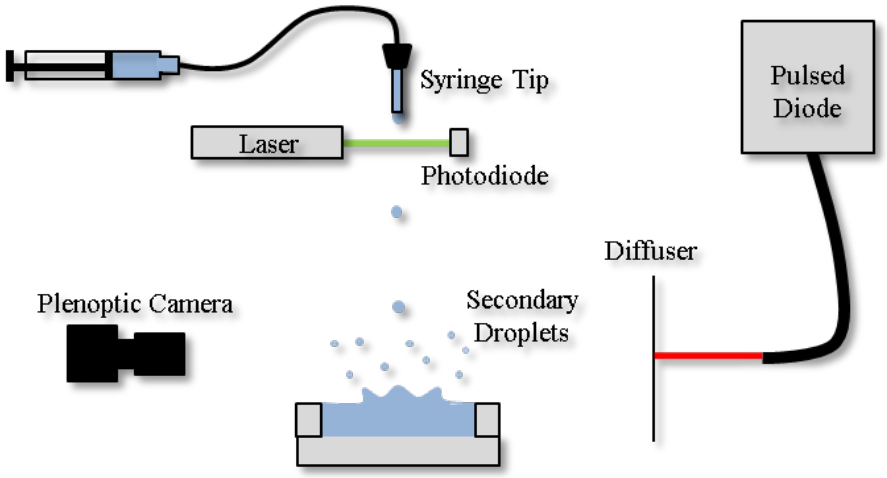

Figure 16: Drop impact configuration

Initial attempts to reconstruct the 3D particle field using image gradient based techniques were complicated by bright spots caused by light refraction through the transparent drops. This was eliminated by coloring the water with black food dye, resulting in nearly opaque droplets. The surface tension of the dyed water was measured to be 0.076 N/m, which is equivalent to that of pure deionized water at the same conditions; therefore, it is assumed that the addition of the food dye does not measurably affect the properties of the fluid.

As in the comparable DIH experiment, each run was characterized by an impact Weber number, *We*, and non-dimensional time, τ, calculated using Equations (19) and (20), respectively.

$$We = \rho v_0^2 d_0/\sigma \tag{19}$$

$$\tau = t v_0/d_0 \tag{20}$$

In these equations and the following discussion, ρ is the drop density assumed to be 1000 kg/m^3, σ is the surface tension, t is the time since impact, v_0 is the impact velocity and d_0 is the initial drop diameter. Due to the slow rate of droplet generation (about 0.06 Hz) it can be assumed that each drop impact occurred on a quiescent surface.

The plenoptic camera was equipped with a 105 mm Nikon macrolens main objective and was positioned to view the impact as shown in Figure 17. To quantify particle velocities, the interline transfer CCD was operated in double exposure mode and the scene was illuminated with a CaviLux pulsed diode with a wavelength of 640 nm (+/-10 nm) and diffuser. The diode produced two short light pulses approximately 400 ns in duration and 150 μs apart. This resulted in pairs of plenoptic images with an interframe time of 150 μs. An example set of image pairs is shown in Figure 17 where each image is refocused to the nominal focal place. The first frame is shown on the left and the second frame is shown on the right.

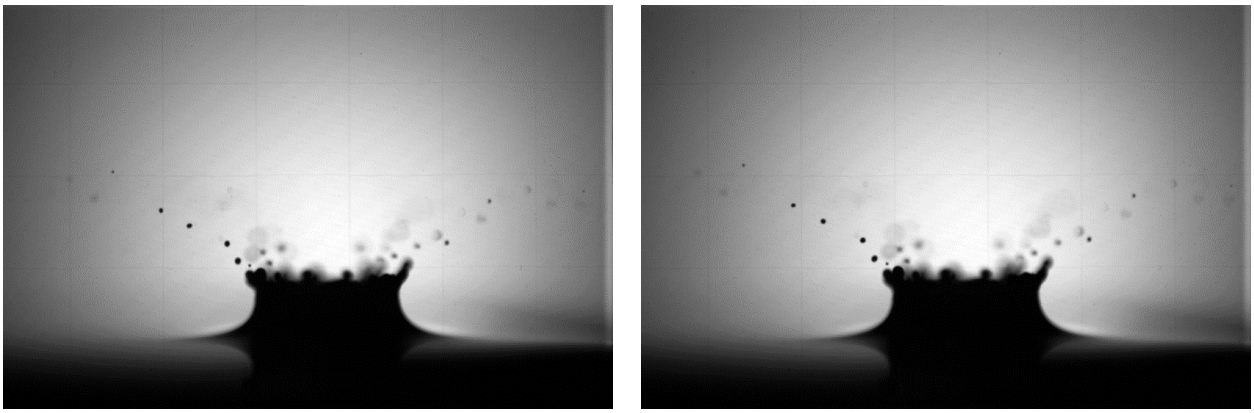

Figure 17: Example drop impact refocused images, frame 1 (left), frame 2 (right)

Finally, a laser and photodiode were used to produce a trigger signal when the falling droplet interrupted the laser beam. This signal provided a trigger to a Stanford Research delay unit (DG645), which triggered the plenoptic camera after a user specified delay. In this experiment the field of view was approximately 29.5 mm by 43.7 mm. The nominal focal plane of the camera was placed at the center of the o-ring.

With this configuration it was possible to investigate different impact velocities by adjusting the height of the syringe tip and different times since impact by adjusting the Stanford delay unit. 250 image pairs were collected at each condition including delay times before and at

the time of impact. The initial analysis presented in section VI.A.1 considers one fall height (roughly 900 mm) and delay time (4 ms since impact). This condition was chosen to closely match the condition investigated in detail using DIH [27]. The other experimental conditions examined in this study are summarized in Table 1. The initial diameter and impact velocities shown were calculated from image pairs captured before the droplet impacted the film and are given as the mean ± standard deviation.

Table 1. Experimental Conditions Examined

Approximate Fall Height (mm)	Initial diameter, d_0 (mm)	Impact Velocity, v_0 (m/s)	Non-Dimensional Time, τ	Impact Weber Number, *We*
600	3.36±0.005	3.74±0.03	2.3±0.01, 4.6±0.03, 6.7±0.04	624±8
900	3.30±0.007	4.24±0.02	2.6±0.01, 5.1±0.03, 7.7±0.04	784±9
1250	3.27±0.016	4.92±0.03	3.0±0.02, 6.0±0.04, 9.0±0.06	1051±14

B. Shotgun Pellet Tracking

Again, the experimental configuration was similar to the previous investigation using DIH [4]. A shotgun (12 gauge, number 9 shot) was placed approximately 4.57 m from the field of view of the plenoptic camera, which was equipped with a 105 mm Nikon macrolens. A break screen was used to trigger the camera as the shotgun pellets passed through the screen. The break screen was placed approximately 18 cm from the center of the field of view of the camera. The pulsed diode and diffuser provided backlight illumination of the pellets, and two images were recorded for each particle field with an interframe time of 5μs. Figure 18 shows a labeled photo of this experimental configuration. The plenoptic camera is located behind the blast shield on the left, viewing the path of the shotgun pellets from the side. According to the manufacturer's

specifications, the shotgun pellets used were 2 mm in diameter. The camera was focused in a plane aligned with the barrel of the shotgun. The field of view of the camera was approximately 86 mm by 127 mm.

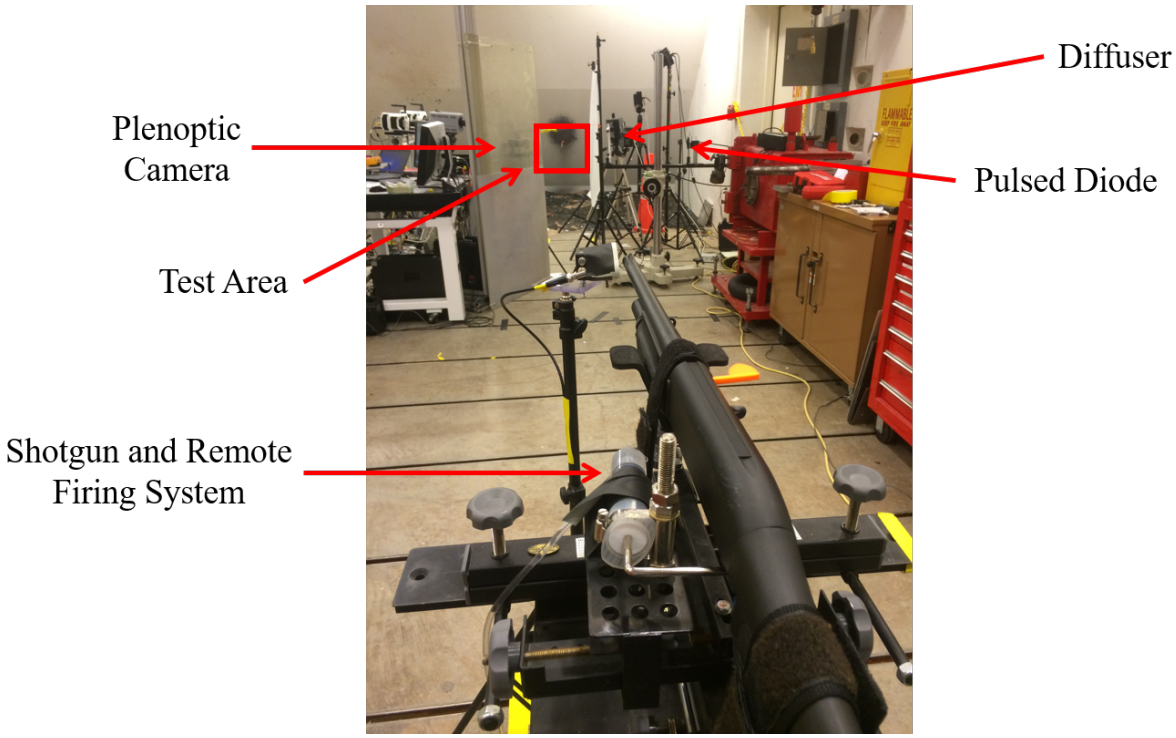

Figure 18: Shotgun pellet tracking configuration

V. Data Processing

The plenoptic images collected in both of these experiments were processed in a similar manner. First, the raw light field data was converted to a volumetric representation of the scene by the creation of stacks of refocused images. Then, particle locations and velocities were determined as described below. Since plenoptic imaging can produce focal stacks similar to the holographic volumes produced in DIH, similar data processing algorithms were used as those used in previous DIH experiments. However, it should be noted that these algorithms may not be taking full advantage of the data collected in light field imaging and more effective algorithms could be created by taking advantage of the perspective view capabilities of plenoptic imaging.

A. Focal Stack Creation

Each raw plenoptic image was processed to create a volume made up of a focal stack. A focal stack is simply a series of refocused images created over a selected depth range. Organizing these images into a 3D volume results in image data represented in voxels, the volume equivalent of a pixel. In these experiments, focal stacks of 1000 images were created. These focal stacks were created using the Light Field Imaging Toolkit (LFIT). An example of this focal stack capability is shown in Figure 19 in which three sample focal planes are displayed from a single instantaneous secondary droplet field.

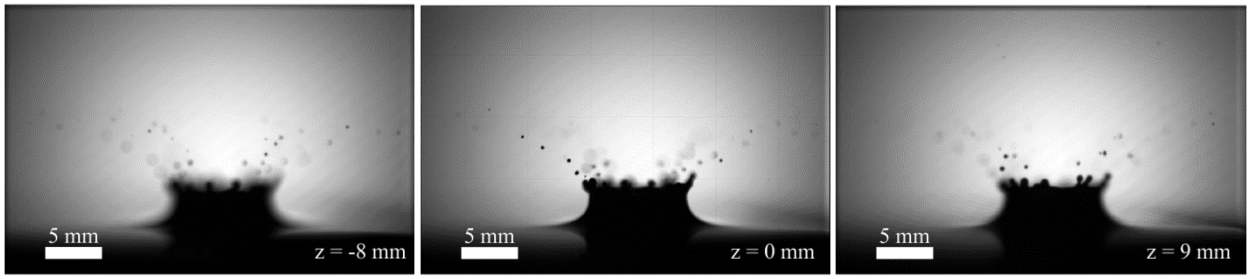

Figure 19: A single raw plenoptic image of a drop impact refocused to three different planes

The focal stacks created in the drop impact experiment were created spanning a depth range of 30 mm in front of and behind the nominal focal plane at the center of the o-ring. These physical depths correspond to alpha values ranging from 0.914 to 1.139 based on the magnification and focal length of the main lens in this experiment. The voxels in this data set had a volume of 0.000143 mm^3, which is representative of the resolution of the data.

The focal stacks created in the shotgun pellet tracking experiment spanned a depth range of 200 mm in front of and behind the nominal focal plane. These physical depths correspond to alpha values of 0.923 to 1.259 based on the magnification and focal length of the main lens in this experiment. The voxels in this data set had a volume of 0.00493 mm^3. The lower resolution of this data set as compared to the drop impact experiment is a result of the significantly larger field of view captured using the same image sensor.

Due to lens distortion in the drop impact experiment it was necessary to dewarp these volumes. The image dewarping function was determined using a 3D second order polynomial fit based on known and measured locations of a dot grid imaged at a variety of depths. The dot card used had a rectangular grid of dots which were 1 mm in diameter and had a spacing of 3 mm between dot centers in both the horizontal and vertical directions. Images of this dot card were captured at locations between 30 mm in front of the focal plane to 30 mm behind the focal plane

in increments of 2.5 mm by moving the dot card on a traverse. A raw image of this dot card located at the nominal focal plane is shown in Figure 20.

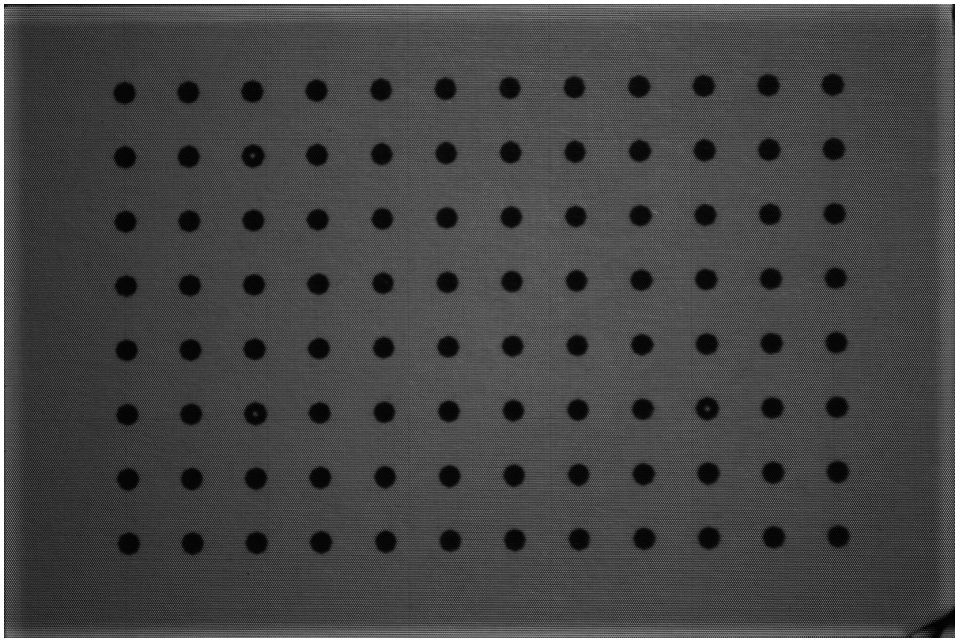

Figure 20: Raw dot card image

A focal stack was created from each of these images and the locations of the dots was measured in each. In several of the focal stacks the dot finding algorithm was unable to locate every dot, therefore, those images were not used in the dewarping function. The remaining 20 sets of detected dots were compiled and identified as the measured dot locations. A corresponding set of known dot locations was created based on the known dot spacing in the x and y directions and the known z location at which the dot card was located in each image. Matrix inversion was then used to solve for a set of coefficients in each dimension using these two sets of dots. The resulting equations were used to relate locations in the original focal stacks to new dewarped locations and a 3D interpolation was used to create new dewarped focal stacks. In the shotgun pellet tracking experiment the volumes were not dewarped to correct for aberrations as no dot card measurements were available. For the present experiment, this is believed to have a minimal effect on the quantified uncertainties. Based on the original measured locations of the dots in the drop impact

experiment compared to the known depth locations, the original average error in the z-direction was approximately 0.8 mm.

B. Particle Identification and Location

1. The Hybrid Method

After dewarping, the 3D location of each particle was measured from the focal stack using a modified version of the processing algorithm defined in Guildenbecher *et al.* 2013, which is a hybrid particle detection method combining minimum intensity and maximum edge sharpness methods. In the minimum intensity method it is assumed that the intensity of the particle is lowest at the in-focus plane, while the maximum edge sharpness method assumes that the sharpness, measured using the Tenengrad operator, is highest at the in-focus plane. Calculation of the Tenengrad operator is shown in Equation (21). This operation is executed for each pixel of each slice of the focal stack resulting in a volumetric sharpness map.

$$T(x,y) = [A(x,y) \otimes S_x]^2 + \left[A(x,y) \otimes S_y\right]^2 \quad (21)$$

In this equation *A(x,y)* is the reconstructed amplitude at the pixel of interest, which is defined as the square root of the pixel intensity. S_x and S_y are horizontal and vertical Sobel kernels at this location. In this previous study it was determined that using a minimum intensity map to locate particles produces accurate shape and in-plane location information while using a measure of maximum edge sharpness is more useful in determining the depth location. These methods were combined by first calculating a minimum intensity map of the volume and applying a variety of thresholds to this map. An optimum threshold was selected to identify a group of possible particles. An example minimum intensity map is shown in Figure 21.

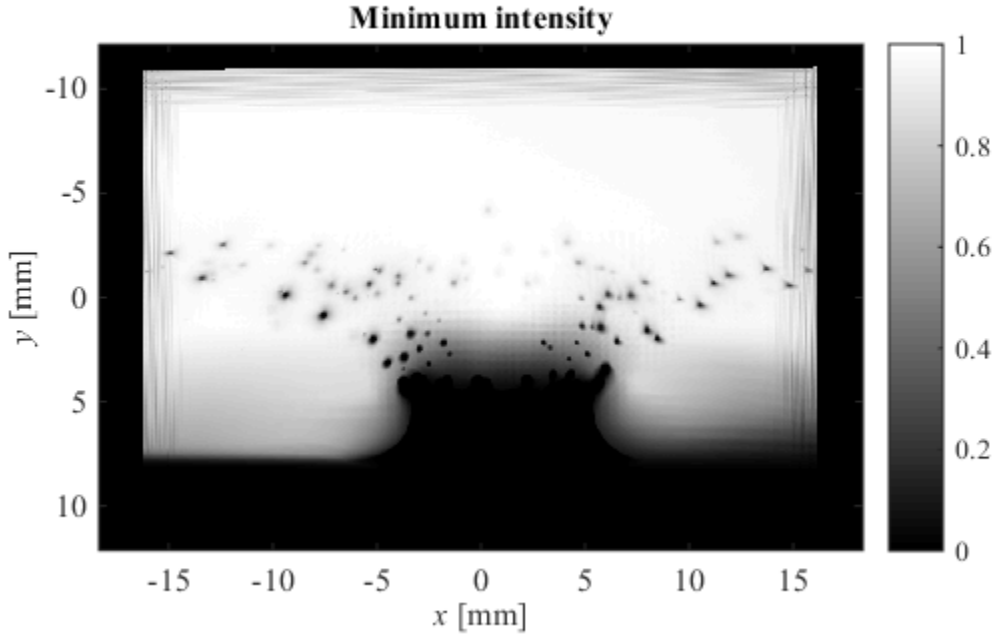

Figure 21: Example minimum intensity map

For every x,y location within the volume the minimum intensity measured at any depth is shown in this plot. Any locations in this plot which have an intensity below the optimum threshold were determined to be possible particles. Then the sharpness for each edge was calculated by averaging the Tenengrad values for the pixels on each edge, and the edge with the maximum sharpness was selected as the in-focus edge. An example maximum Tenengrad map for the same image is shown in Figure 22.

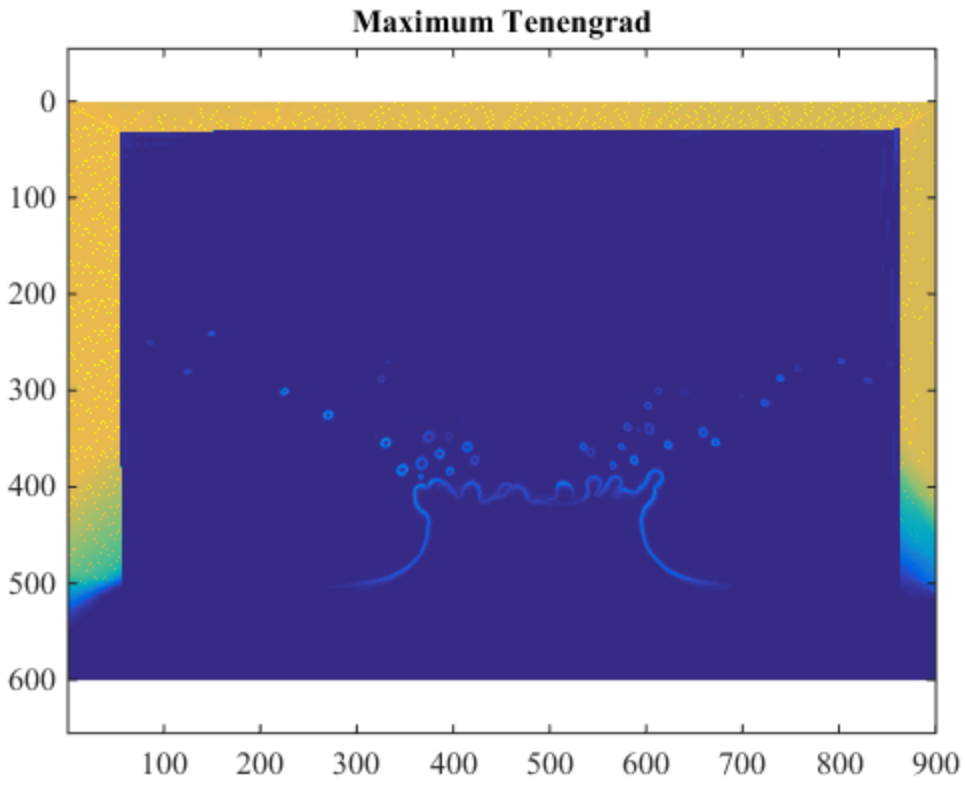

Figure 22: Example maximum Tenengrad map

The depth was then determined from the average depth location of the selected edge [26]. It should be noted that the large areas around the edges and within the crown of the splash also have high Tenengrad values and small minimum intensities. To avoid identifying these regions as particles limitations on the possible size of particles were applied.

2. Challenges and Solutions

Due to limitations of the configuration of these particular experiments we were unable to achieve consistent illumination over the entire field of view, resulting in images which were much darker around the edges than in the center. Therefore when a single intensity threshold was used for a particular image, very few particles were initially detected. To correct this problem an additional processing step was included in which the images were divided into smaller regions and

an optimum intensity threshold was selected for each region. Using these varied thresholds the group of possible particles was detected. Then, as before, the maximum edge sharpness portion of the algorithm was executed.

Once located in 3D space, individual diameters were measured from the refocused image of each particle. Finally, particle velocities were determined based on a nearest neighbor matching between the 3D particles fields recorded with a short interframe time as described in Chapter IV.

C. Computational Requirements

Processing the data collected in these experiments required significant computational resources, particularly in the drop impact experiment as 7500 images were collected. In the shotgun experiment considerably fewer images were collected as execution of only a limited number of shotgun firings was logistically feasible. The image processing was executed using a computer cluster and up to 200 cores simultaneously. On a single core, each image required approximately 10 hours of computational time. In future work, this time may be substantially reduced by improvement of the efficiency of the existing algorithm as well as the implementation of other algorithms, possibly utilizing the perspective shift capabilities of plenoptic imaging, which can be computed significantly faster.

VI. Results and Discussion

The most striking result of the analysis of the data collected in these two experiments using plenoptic imaging and digital in-line holography has been that the quality of the results produced is highly dependent on the specific experimental parameters. Though informative analysis was obtained in every experiment, the significance of the benefits of each method differed based on elements such as the size of the particles examined, the compressibility of the flow field, and the size of the region of interest.

A. Drop Impact Experiment

1. Example Plenoptic Imaging Results

Figure 23 displays two orthogonal views of the measured secondary fragments and their velocities for a sample drop impact case with We = 784 and τ = 5.1. This particle field was quantified from the images shown in Figure 19. The initial drop diameter (3.3 mm) and the impact velocity (4.24 m/s) were calculated from a set of image pairs taken immediately before impact. As expected the secondary droplets generally move radially outward, with uncertainty that appears higher in the out-of-plane, z, direction compared to the in-plane x and y directions. In comparing these results to the similar DIH case, both show similar droplet motion and size, however, in the DIH case 196 droplets are identified per realization while in the plenoptic case only 45 droplets are identified per realization. This difference can likely be attributed to the lower spatial resolution of the current plenoptic imaging configuration (49 μm per refocused pixel) compared to the DIH configuration (7.4 μm per pixel). In addition, in this preliminary investigation the plenoptic data has been processed using algorithms adapted from DIH. In the future, it might be possible to define

algorithms specifically for plenoptic data which may improve these results, such as the use of perspective views to make use of the light field data contained in those images or deconvolution to remove unwanted blurring [28].

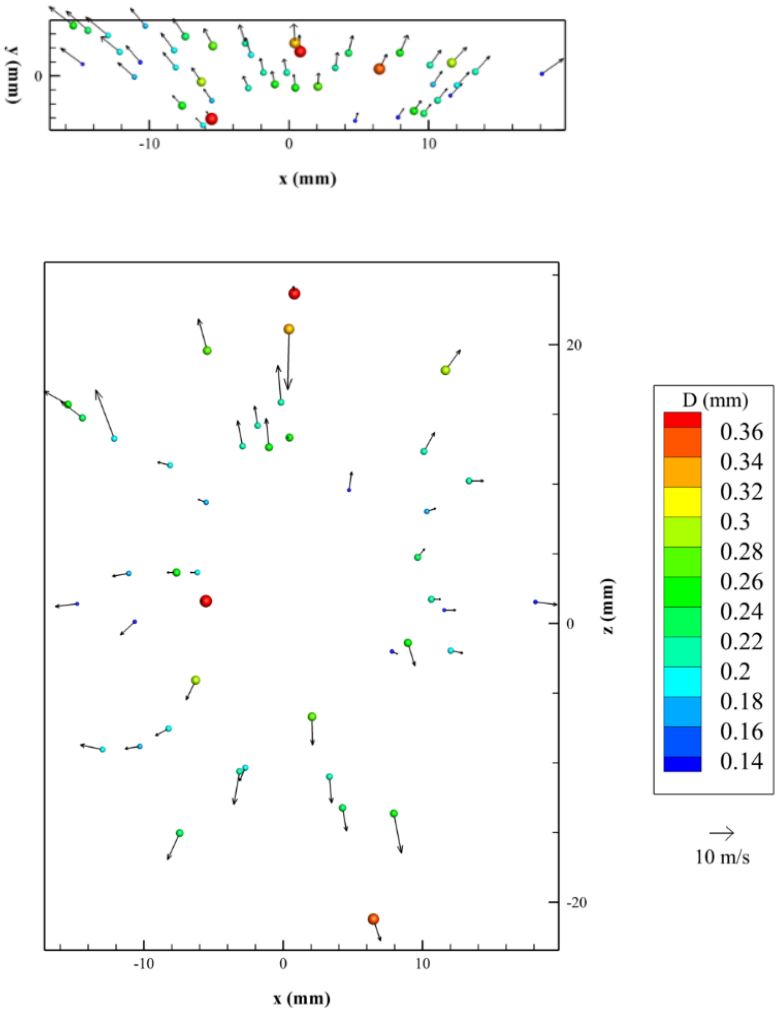

Figure 23: Measured three dimensional droplet sizes and velocities

Figure 24 shows a histogram of the measured drop size from all realizations at We = 784 and τ = 5.1. A notable feature of this data appears in the clipped shape of the lower end of the histogram. This clipping is due to the resolution limit of the plenoptic camera. In this experiment a pixel was approximately 49 μm, therefore, particles with a diameter approaching this value were not captured using this system.

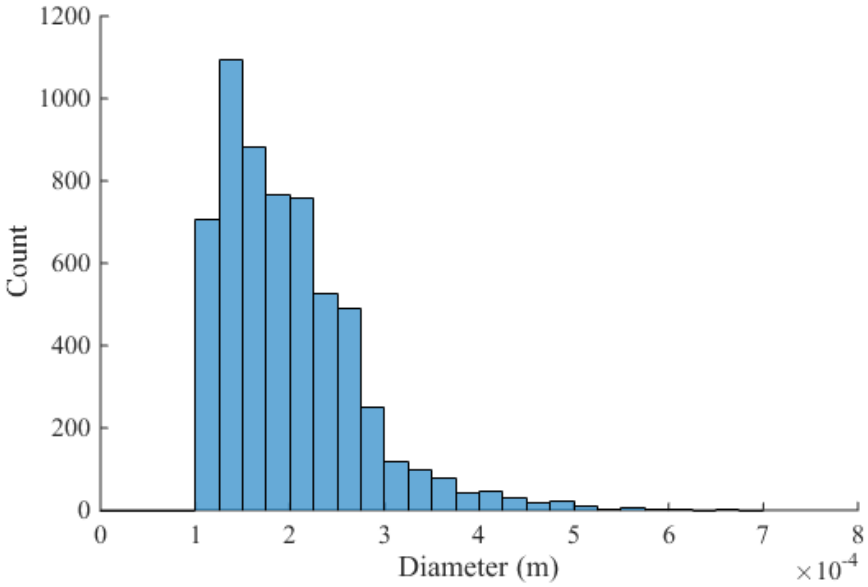

Figure 24: Measured drop size histogram

Figure 25 displays the x and z displacement components from measured secondary droplets at We = 784 and τ = 5.1. Displacement in each of these dimensions is plotted as a function of the distance from the impact center. Linear fits of the x and z displacements are also plotted in this figure. The agreement of these two linear fits shows that the mean measured displacements in the x and z directions are similar as expected due to flow symmetry. It should be noted that only 10 % of the measured droplets are shown in this plot for clarity, however, all calculations include all data points. Model error is defined as the difference between the measured displacement component and the displacement component predicted by the linear fit at the measured position.

The standard deviation of the model error is calculated to be 0.263 mm for x and 0.411 mm for z. The difference in these values can be used to approximate the depth uncertainty of the technique by assuming negligible uncertainty in the x direction. This results in a z positional uncertainty of approximately 0.75 mean measured particle diameters, based on the average particle diameter of 0.199 mm. For the comparable DIH case, the standard deviation of z positional uncertainty was determined to be 0.72 mean measured particle diameters, while over a broader range of experiments the depth uncertainty of DIH was determined to be approximately 1-2 particle diameters [23]. In general, it appears for the conditions and processing methods considered here both DIH and plenoptic imaging give similar depth uncertainties. Detailed results from the other experimental conditions tested are examined in the Appendix.

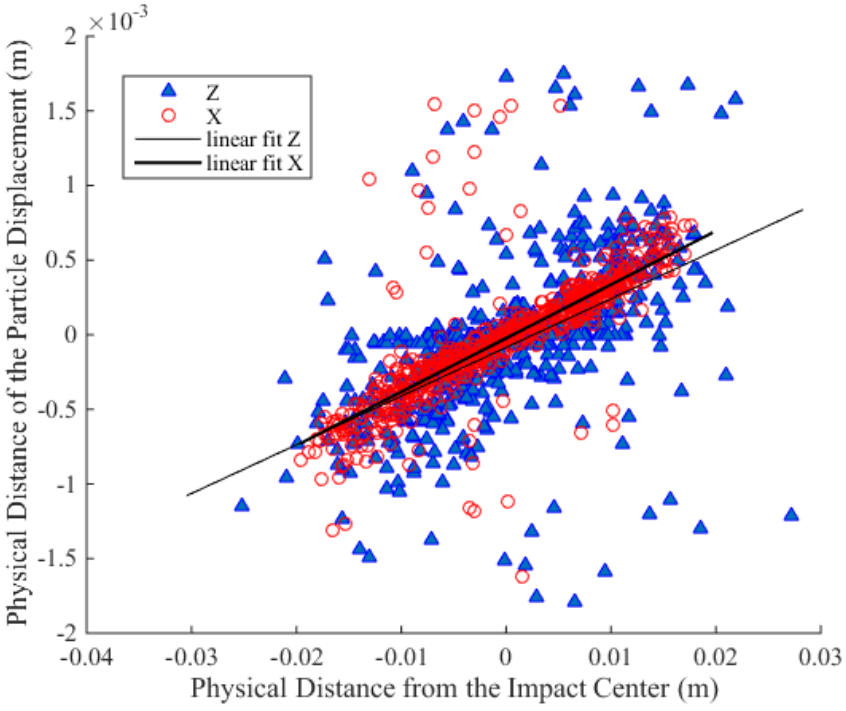

Figure 25: Measured particle displacements

2. Depth Uncertainty

To better understand the main sources of uncertainty in plenoptic imaging, this experiment was repeated at three fall heights and three delay times for a total of nine different conditions. In all cases, the standard deviation in model errors was calculated as above. These model error standard deviations, as well as the calculated *z* uncertainties, are shown in Table 2 and are shown in physical units for clarity. Our initial analysis indicates that the standard deviation in model errors varies significantly in the *x* direction, while the standard deviation in model errors in the *z* direction is roughly unchanged as a function of experimental conditions. This suggests that the calculated standard deviations in the *z* direction may be constrained by the depth of field of the imaging system and indicates the *z* positional uncertainty may be strongly related to this quantity.

Table 2. Model error standard deviations and depth uncertainties

Drop Height (mm)	Delay Time (ms)	Standard Deviation of the x Model Error (mm)	Standard Deviation of the z Model Error (mm)	z Uncertainty (mm)
600	233	0.275	0.392	0.116
	235	0.110	0.341	0.232
	237	0.070	0.354	0.285
900	318	0.437	0.445	0.008
	320	0.263	0.411	0.148
	322	0.103	0.373	0.271
1250	402	0.312	0.393	0.081
	404	0.182	0.365	0.183
	406	0.093	0.347	0.255

Examination of the theoretical depth resolution limits of each method can provide some insight into the validity of these experimentally determined uncertainties. The theoretical depth resolution of a plenoptic system is determined by Equation (22) derived by Deem *et al* [29].

$$\delta z = \frac{d_M\left(1-\frac{2}{N_p}\right)}{2tan\left(\frac{d_M\left(1-\frac{2}{N_p}\right)}{2f_M}-tan^{-1}\left(\frac{d_M\left(1-\frac{2}{N_p}\right)+d_\mu}{2s_i}\right)\right)}-\frac{d_M}{2tan\left(\frac{d_M}{2f_M}-tan^{-1}\left(\frac{d_M+d_\mu}{2s_i}\right)\right)} \quad (22)$$

As shown in this equation, the depth resolution, δz, is a function of the main lens diameter, d_M, the number of pixels behind each microlens, N_p, the diameter of the microlenses, d_μ, the main lens focal length, f_M, and the image distance, s_i. As would be expected, the depth resolution improves as the number of pixels behind each microlens increases and the microlens diameter increases. The limiting case on depth resolution is the conventional depth of field of the main lens when the circle of confusion is the microlens diameter. Additionally, it should be noted that the depth resolution varies with axial position and Equation (22) represents the worst case resolution, which occurs at the nominal focal plane. The depth resolution is the worst at the nominal focal plane because rays emanating from this depth impact only one microlens. The other practical limitation on the depth resolution is the bit depth of the imaging system. Deem *et al* has shown that a higher bit depth and therefore a larger dynamic range will result in improved depth resolution [29]. For the camera parameters in this experiment the theoretical depth resolution is approximately 0.24 mm according to Equation (22). Comparison of this value to those in Table 2 shows some discrepancy. This discrepancy is likely due to the assumptions in the model, which defines the resolution at the worst case axial location, as well as scatter in the data. The model generally predicts the magnitude of the uncertainty relatively well particularly at the larger delay times. More work is needed to fully quantify these observations.

Figure 26 shows the ratio of z uncertainty to particle diameter plotted as a function of particle diameter for all of the cases examined. Overlaid on this plot is the theoretical trend

determined using the calculated theoretical depth resolution. This plot demonstrates the significant scatter from the expected trend in the collected data.

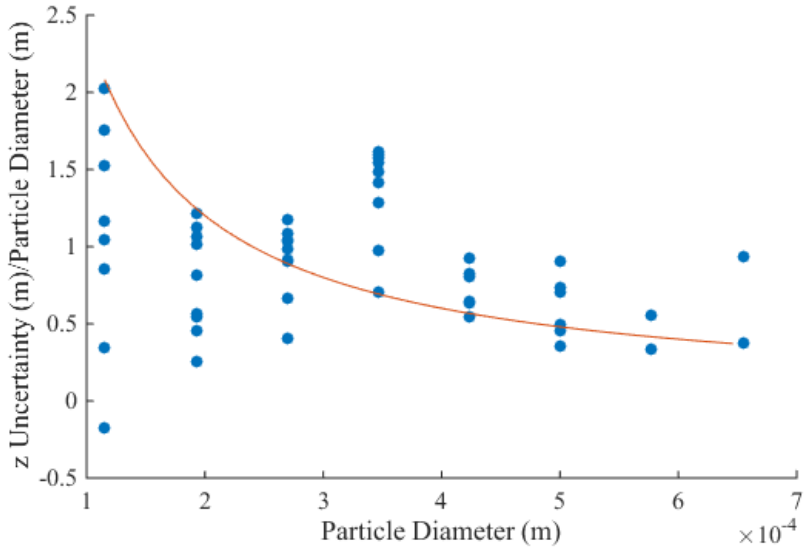

Figure 26: Plenoptic depth uncertainty-particle diameter relationship

The theoretical depth resolution of DIH is defined by Equation (23), where d is the particle diameter and λ is the wavelength of the illumination light.

$$\Delta z = \frac{d^2}{\lambda} \tag{23}$$

Based on this measure, the depth uncertainty increases as particle size increases, however, it should be noted that the constant of proportionality in this relationship is highly dependent on the image processing algorithm used [2]. This dependence is apparent in the plot shown in Figure 27. Similarly to Figure 26, this figure shows the ratio of z uncertainty to particle diameter plotted as a function of particle diameter for all of the cases examined in the DIH experiment. According to this data set, the uncertainty decreases with increasing particle diameter. This decrease is likely the result of the edge sharpness criteria used to locate particles. Since larger particles cover more image pixels there are more edge pixels and therefore more contributions to the averaging scheme.

This larger amount of data then results in lower depth uncertainty measurements as individual erroneous measurements become less significant.

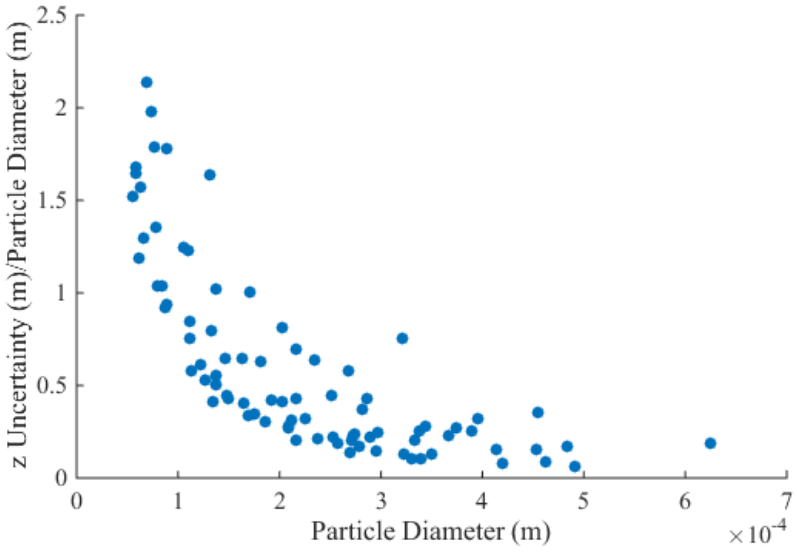

Figure 27: DIH depth uncertainty-particle diameter relationship

3. Effect of Weber Number and Delay Time

Figure 28 (left) displays the average secondary droplet diameter, normalized by the initial diameter, detected for each experimental configuration. The error bars in this plot show the range of one standard deviation on either side of the average. Symbols show the average for each experimental condition and lines show a power law fit to the experimental results for each Weber number. Like the comparable DIH experiments examined in Guildenbecher *et al* [27], this plot shows that secondary droplet diameter generally follows a power law relationship with increasing time given by $d/d_0 = q\tau^n$, though there is some disagreement in the values of q and n between the techniques. This is likely due to the increased scatter in the plenoptic data.

Similarly, Figure 28 (right) shows the average radial velocity, normalized by the impact velocity, detected for each experimental configuration. In comparing this plot to the similar DIH results [27] we see in both data sets that radial velocity decreases with time after impact.

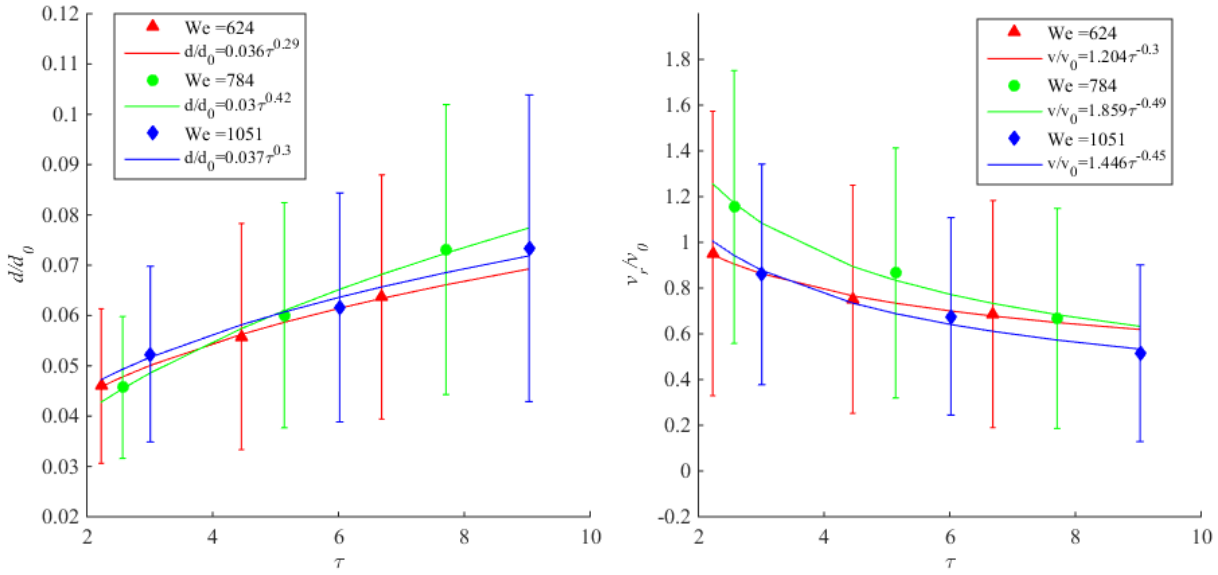

Figure 28: Normalized average measured diameter (left) and normalized radial velocity (right) as a function of non-dimensional delay time

Examining similar plots for the two horizontal velocity components demonstrates the discrepancy we've seen in these two directions. Figure 29 (left) shows a plot of the normalized x velocity components and Figure 29 (right) shows a plot of the normalized z velocity components, the expected decrease is much more obvious in the x component though there is still a decreasing trend in the z direction. This suggests higher accuracy on the x direction as the trend is closer to the expected decrease. Again, the error bars in this plot show the range of one standard deviation on either side of the average and symbols show the average for each experimental condition. Lines show a power law fit to the experimental results for each Weber number.

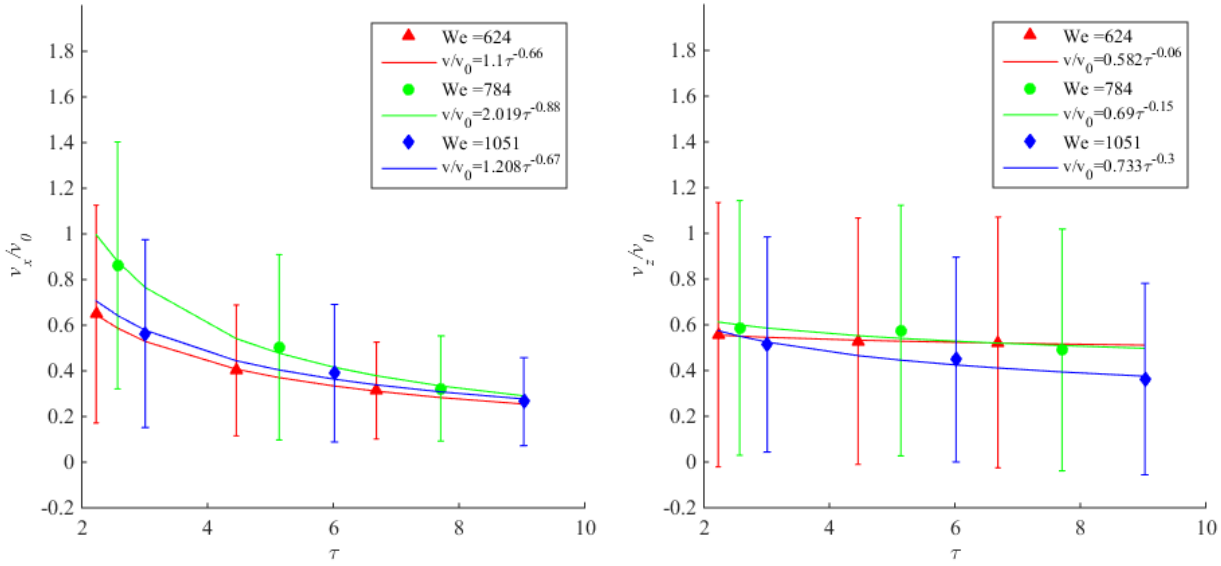

Figure 29: Normalized x velocity (left) and normalized z velocity (right) as a function of non-dimensional delay time

B. Shotgun Pellet Tracking

1. Compressibility Artifacts

Figure 30 shows a plenoptic image pair refocused to two different depths. In these images the pellets propagate right to left. The two images on the left show frames 1 and 2 refocused near the front of the volume while the two images on the right show frames one and two refocused near the back of the volume. Figure 31 shows a DIH image pair similarly refocused to two different depths. Visual comparison of these figures provides a qualitative comparison of the two imaging methods. The vertical bands in the DIH images are a result of shockwaves visible due to the use of collimated laser light used for illumination. This image artifact is not observed in the plenoptic results because they were recorded using diffuse white light. This artifact reduction highlights a significant benefit of plenoptic imaging.

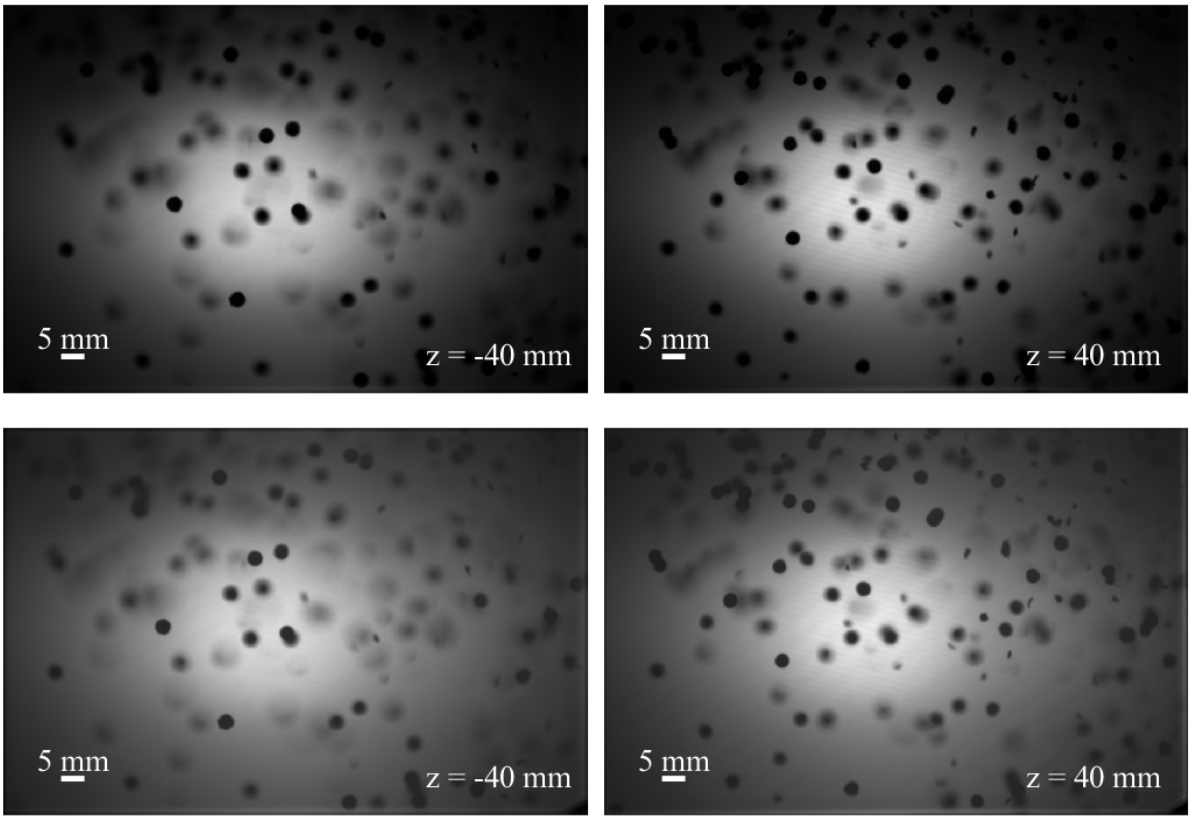

Figure 30: Refocused plenoptic shotgun blast images

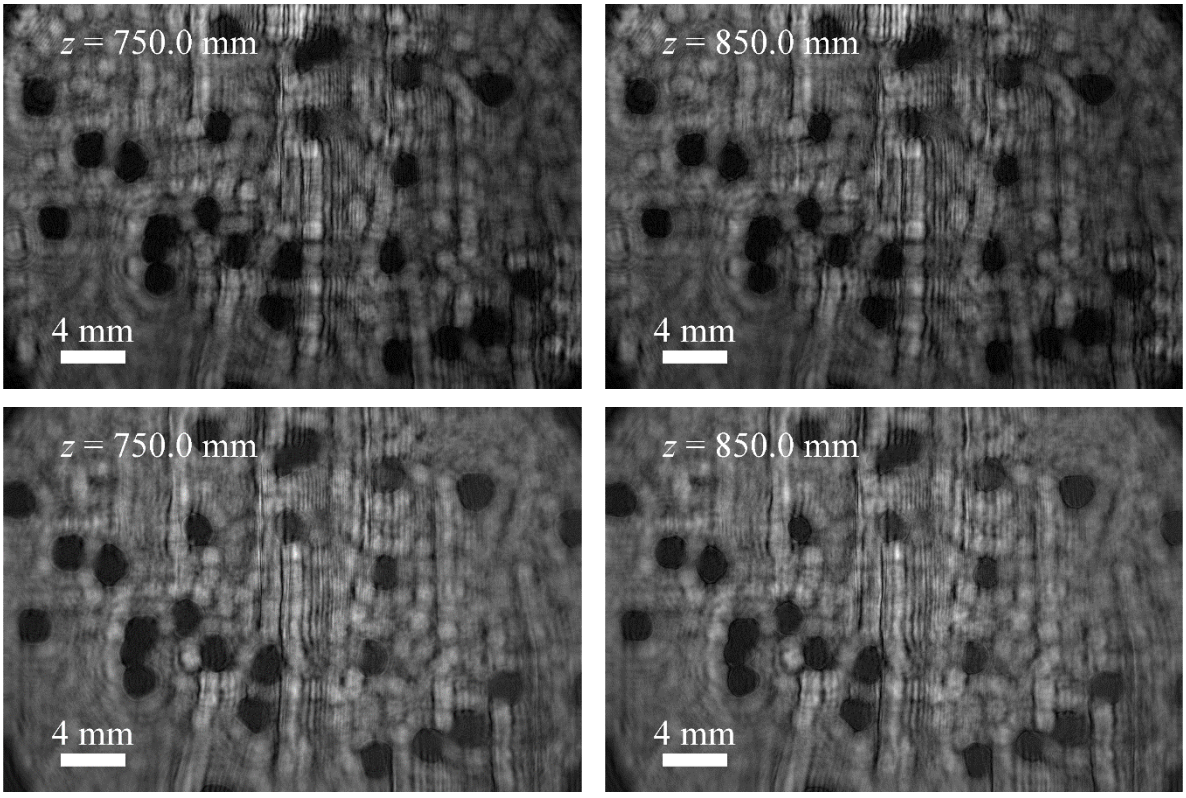

Figure 31: Refocused DIH shotgun blast images

2. Field of View

Another significant difference, which can be seen in these figures, is the difference in field of view which can be visualized using each method. The field of view used in DIH is limited by the size of collimation lenses, which are difficult and costly to obtain at diameters greater than approximately 50 mm. On the other hand, the field of view of the plenoptic camera can be readily changed by adjusting the focus of the main objective (which, of course, also affects the minimum spatial resolution).

3. Size and Location Accuracy

Figure 32 shows a 3D representation of the measured pellet size and motion from one realization. As expected, the pellets move primarily in the horizontal, x, direction, though some uncertainty in the depth, z, direction is apparent.

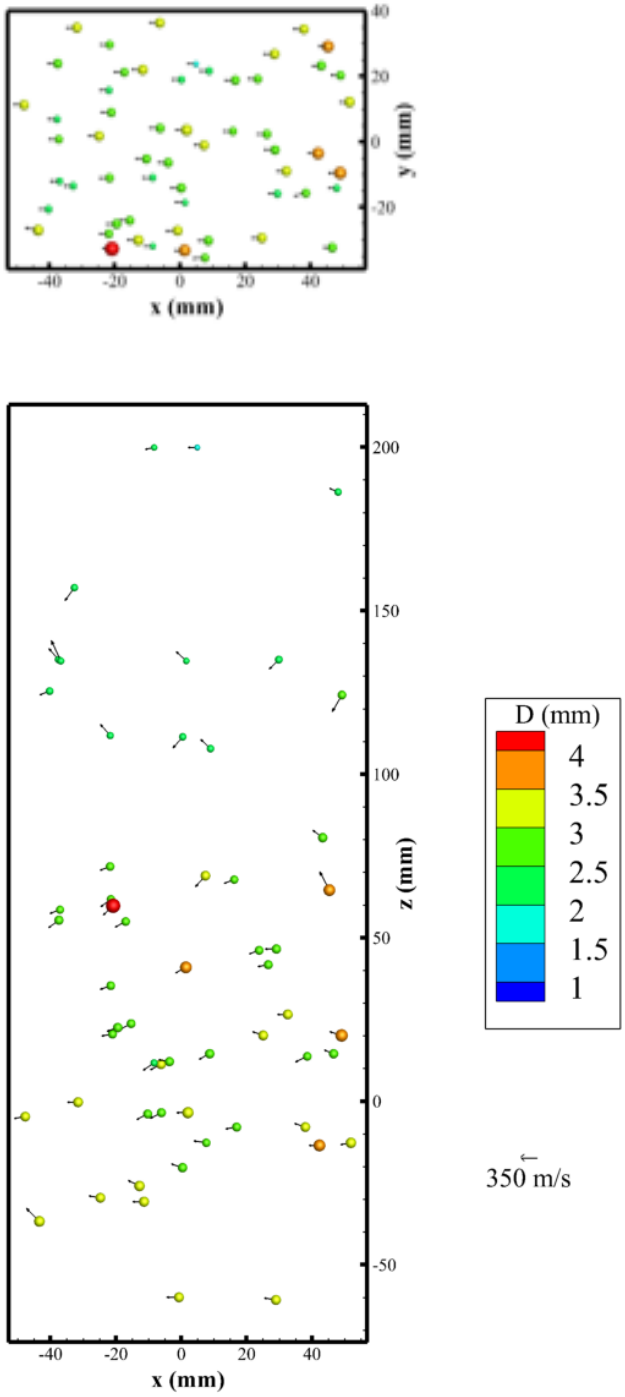

Figure 32: Shotgun experiment vector plot

The mean particle diameter measured from all realizations is 2.1743 mm with a standard deviation of 0.7836 mm. This is in agreement with expected pellet diameter of approximately 2 mm as defined by the manufacturer specifications. The relatively large standard deviation may arise partly from variations in the actual pellet diameters as well as the incorrect identification of small pieces of the break screen as pellets or overlapping pellets as a single particle. Further refinement of the processing algorithms may reduce this standard deviation.

Figure 33 displays a histogram of the displacement in the *z* direction calculated using the detected particle matches; the mean displacement is -0.13 mm with a standard deviation of 1.59 mm. This results in an uncertainty, quantified by the standard deviation, of 0.74 mean particle diameters, which is again in reasonable agreement with previous estimates of DIH uncertainty of around 1-2 particle diameters.

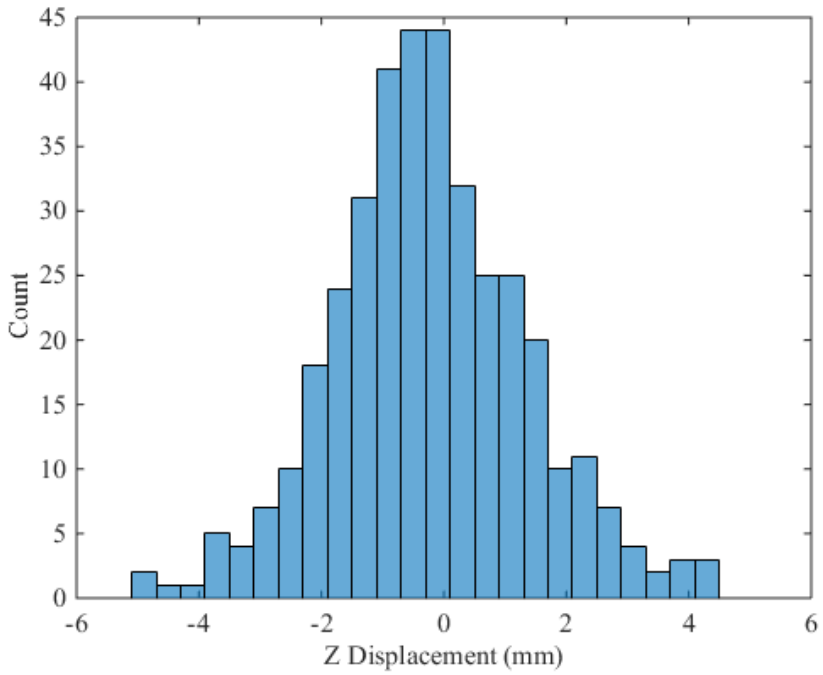

Figure 33: Z displacement histogram

VII. Conclusions

This work presents a preliminary comparison of diagnostics for measurement of particle size, positions, and velocities in a 3D volume. Digital in-line holography (DIH) is an established technique that reconstructs a 3D volume by numerically refocusing laser diffraction patterns. On the other hand, plenoptic imaging is an emerging technique that utilizes a microlens array to encode angular information of a light field. In this work, plenoptic imaging is applied to quantify the secondary fragments from the impact of a water drop on a thin film of water and the high-speed particles from a shotgun. Results are compared to previous measurements of these flows using DIH. Each technique is shown to have certain advantages and challenges as summarized in Table 3.

Table 3. Strengths and weaknesses of each technique

	Advantages	Challenges
Plenoptic Imaging	• Simple experimental setup requiring limited optical access • Can utilize diffuse, white light illumination sources	• Lower effective spatial resolution • Data processing techniques are not fully developed • Requires custom imaging hardware
Digital In-line Holography (DIH)	• Well established technique, including mature data processing methodology • High spatial resolution • Utilizes commercial hardware, including possibility of high-speed imagers	• Requires collimated laser illumination, which increases experimental complexity and can cause unwanted artifacts

Several other specific conclusions can be drawn as a result of these experiments. Both DIH and plenoptic imaging are capable of measuring the 3D nature of the chosen particle fields. This includes an ability to quantify a particle size distribution in a large volume, measure instantaneous

3D position and three-component particle velocities, and reconstruct the expected flow symmetries. Both DIH and plenoptic imaging suffer from higher positional uncertainty in the direction normal to the imaging plane. For the configurations and processing algorithms considered here, the out-of-plane positional uncertainty of plenoptic imaging is shown to be around 1 mean particle diameter. This is similar to previous estimates of DIH positional uncertainty of around 1-2 mean particle diameters. For a fixed image sensor, DIH tends to have higher spatial resolution compared to plenoptic imaging. As shown in the drop impact results, this limits the dynamic range of particle sizes, which can be quantified in a single experiment. By utilizing diffuse light sources, plenoptic imaging is less susceptible to image distortion through index of refraction gradients compared to DIH, which requires collimated and coherent illumination. This is illustrated in the experiments investigating shotgun pellets. The DIH results show clear image distortion due to gas phase shockwaves that exist between the particles, while this effect is not observed in the corresponding plenoptic measurement.

It should also be noted that these experiments do not address all limitations of either technique. In particular, both measurement techniques are challenged when the particle number density increases. More work is needed to determine which, if any, technique is advantageous at high particle densities. In addition, each method currently requires significant computational resources, necessitating the use of a computer cluster to reasonably process the desired volume of data. Although, the algorithms currently implemented have not been optimized for computational efficiency and these requirements are expected to be significantly reduced as improvements are made.

References

[1] F. Scarano, "Tomographic PIV: principles and practice," *Meas. Sci. Technol.*, vol. 24, p. 012001, 2012.

[2] J. Katz and J. Sheng, "Applications of Holography in Fluid Mechanics and Particle Dynamics," *Annu. Rev. Fluid Mech.*, vol. 42, pp. 531–555, 2010.

[3] J. Gao, D. R. Guildenbecher, P. L. Reu, V. Kulkarni, P. E. Sojka, and J. Chen, "Quantitative, three-dimensional diagnostics of multiphase drop fragmentation via digital in-line holography.," *Opt. Lett.*, vol. 38, no. 11, pp. 1893–5, 2013.

[4] D. R. Guildenbecher, P. L. Reu, H. L. Stuaffacher, and T. Grasser, "Accurate measurement of out-of-plane particle displacement from the cross correlation of sequential digital in-line holograms," *Opt. Lett.*, vol. 38, no. 20, p. 4015, 2013.

[5] C. Tropea, A. L. Yarin, and J. F. Foss, Eds., *Springer Handbook of Experimental Fluid Mechanics*. Berlin: Springer-Verlag, 2007.

[6] K. Hoyer, M. Holzner, B. Lüthi, M. Guala, A. Liberzon, and W. Kinzelbach, "3D scanning particle tracking velocimetry," *Exp. Fluids*, vol. 39, no. 5, pp. 923–934, 2005.

[7] E. Adelson and J. Bergen, "The plenoptic function and the elements of early vision," *Comput. Model. Vis. ...*, pp. 3–20, 1991.

[8] H. Meng, G. Pan, Y. Pu, and S. H. Woodward, "Holographic particle image velocimetry: from film to digital recording," *Meas. Sci. Technol.*, vol. 15, pp. 673–685, 2004.

[9] T. Kreis, *Holographic Interferometry Principles and Methods*. Berlin: Akademie Verlag, 1996.

[10] E. Adelson and J. Bergen, “The plenoptic function and the elements of early vision,” *Comput. Model. Vis. ...*, pp. 3–20, 1991.

[11] E. H. Adelson and J. Y. a Wang, “Single lens stereo with a plenoptic camera,” *IEEE Trans. Pattern Anal. Mach. Intell.*, vol. 14, no. 2, pp. 99–106, 1992.

[12] M. Levoy, “Light Fields and Computational Imaging,” *IEEE Comput. Soc.*, pp. 46–55, 2006.

[13] R. Ng, M. Levoy, G. Duval, M. Horowitz, and P. Hanrahan, “Light Field Photography with a Hand-held Plenoptic Camera,” *Informational*, pp. 1–11, 2005.

[14] T. W. Fahringer, K. P. Lynch, and B. S. Thurow, “Volumetric particle image velocimetry with a single plenoptic camera,” *Meas. Sci. Technol.*, vol. 26, no. 11, p. 115201, 2015.

[15] A. Bichal, “Development of 3D Background Oriented Schlieren with a Plenoptic Camera,” Auburn University, 2015.

[16] R. J. Collier, C. B. Burckhardt, and L. H. Lin, *Optical Holography*. New York: Academic Press, 1971.

[17] C. M. Vest, *Holographic Interferometry*. New York: John Wiley and Sons Inc., 1979.

[18] P. Hariharan, *Optical holography*. Australia: Press Syndicate of the University of Cambridge, 1984.

[19] K. D. Hinsch and S. F. Herrmann, “Holographic particle image velocimetry,” *Meas. Sci. Technol.*, vol. 15, 2004.

[20] W. Schumann and M. Dubas, *Holographic Interferometry*. New York: Springer Verlag, 1979.

[21] J. B. DeVelis, G. O. Reynolds, B. J. Thompson, G. April, and H. H. Arsenault, *Handbook of Optical Holography*. New York: Academic Press, 1979.

[22] K. Lynch, “Development of a 3-D Fluid Velocimetry Technique based on Light Field Imaging,” Auburn Univeristy, 2011.

[23] J. Gao, D. R. Guildenbecher, P. L. Reu, and J. Chen, “Uncertainty characterization of particle depth measurement using digital in-line holography and the hybrid method,” vol. 21, no. 22, pp. 17512–17517, 2013.

[24] Y. Pu and H. Meng, “Four-dimensional dynamic flow measurement by holographic particle image velocimetry.,” *Appl. Opt.*, vol. 44, no. 36, pp. 7697–7708, 2005.

[25] H. Meng, W. L. Anderson, F. Hussain, and D. D. Liu, “Intrinsic speckle noise in in-line particle holography,” *J. Opt. Soc. Am. A*, vol. 10, no. 9, p. 2046, 1993.

[26] D. R. Guildenbecher, J. Gao, P. L. Reu, and J. Chen, “Digital holography simulations and experiments to quantify the accuracy of 3D particle location and 2D sizing using a proposed hybrid method,” *Appl. Opt.*, vol. 52, no. 16, pp. 3791–3801, 2013.

[27] D. R. Guildenbecher, L. Engvall, J. Gao, T. W. Grasser, P. L. Reu, and J. Chen, “Digital in-line holography to quantify secondary droplets from the impact of a single drop on a thin film,” *Exp. Fluids*, vol. 55, 2014.

[28] J. T. Bolan, “Enhancing Image Resolvability in Obscured Environments Using 3D Deconvolution and a Plenoptic Camera,” Auburn University, 2015.

[29] E. A. Deem, L. N. Cattafesta, T. W. Fahringer, and B. S. Thurow, “On the resolution of Plenoptic PIV,” in *11th International Symposium on Particle Image Velocimetry*, 2015.

[30] G. E. Cossali, M. Marengo, A. Coghe, and S. Zhdanov, “The role of time in single drop splash on thin film,” *Exp. Fluids*, vol. 36, no. 6, pp. 888–900, 2004.

Appendix

This appendix gives detailed results for each of the configurations examined in the drop impact experiment, similar to those presented in section VI.A.1 for a single configuration. These configurations include three different drop heights and three different delay times. The condition examined previously is repeated here for completeness. The trials are defined by the corresponding Weber number and non-dimensional time as defined in Equations (19) and (20) respectively. As in the example case, all the scatter plots of measured particle displacements shown here display on 10 % of the data points for clarity, however, the best fit lines and uncertainty calculations were determined based on all data points.

Several general observations can be made in comparing the results from each configuration. In the configurations in which the data was collected at a larger delay time after impact, the incidence of larger particle diameters increases. This increase is more significant at higher Weber numbers. These observations are consistent with the expected development of a secondary particle field created by a drop impact [30].

Although the same number of images was collected in each configuration, the data sets differ significantly in the total number of particles that were measured. Due to this difference in the amount of data available, some data sets provide more statistically significant information than others. The differences in the amount of particles detected can be attributed to two main sources. First, the different configurations result in secondary particle fields in a wide range of developmental stages, some of which have many more secondary droplets than others. Second, as previously noted, the image processing algorithms used in this work are adapted from those used

in DIH, therefore, development of algorithms more specifically tailored to light field data could increase the number and size range of particles which can be detected in the plenoptic experiments.

Overall, the statistical results calculated in each of these data sets are in general affected more significantly by increases in the delay time after drop impact than by changes in the Weber number.

1. We = 624, τ = 2.3

The histogram in Figure 34 shows that the particle diameters detected in this configuration are in the expected range. It should also be noted from this figure that a relatively small number of particles was detected, which may reduce the significance of the statistics determined from this individual data set.

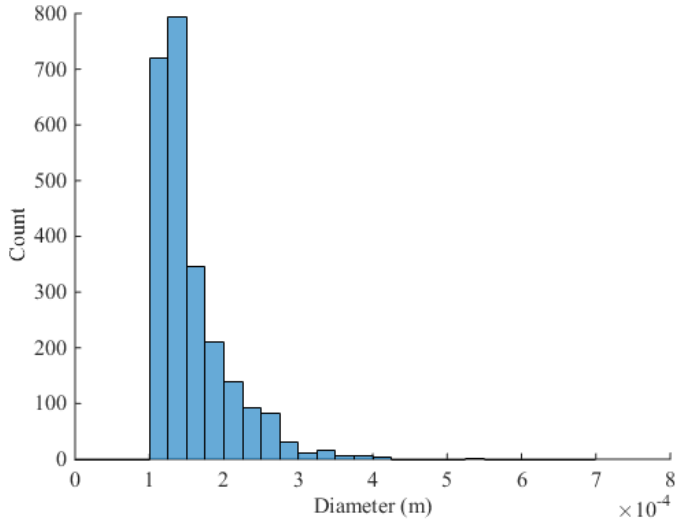

Figure 34: Measured drop size histogram

Figure 35 shows the measured particle displacements for this configuration. This data set shows significant scatter in both the X and Z directions, which contributes to the small calculated Z positional uncertainty of 0.116 mm.

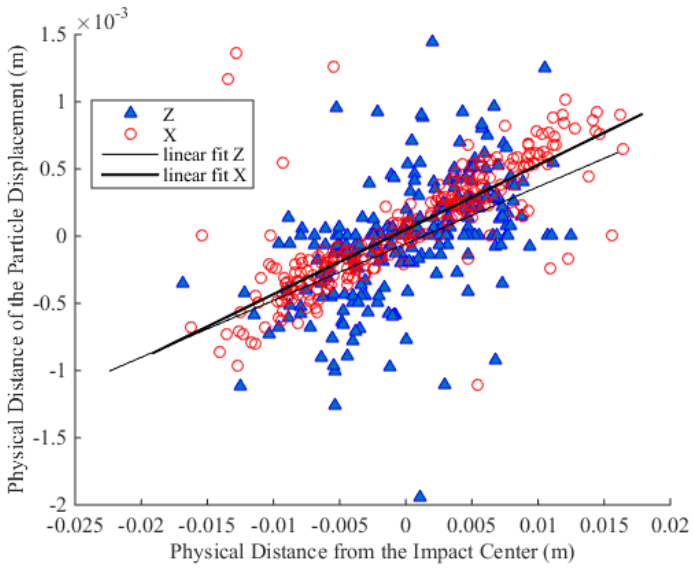

Figure 35: Measured particle displacements

2. We = 624, τ = 4.6

This configuration is at the same Weber number as the previous, however, the images were captured at a larger delay time. In comparing the measured drop size histogram for this configuration, shown in Figure 36, to the previous configuration, the increase in the number of larger diameter particles is apparent as a large number of particles are detected up to approximately 0.3 mm. Comparing the overall counts in this histogram to that of the previous configuration also shows that significantly more particles were detected in this case.

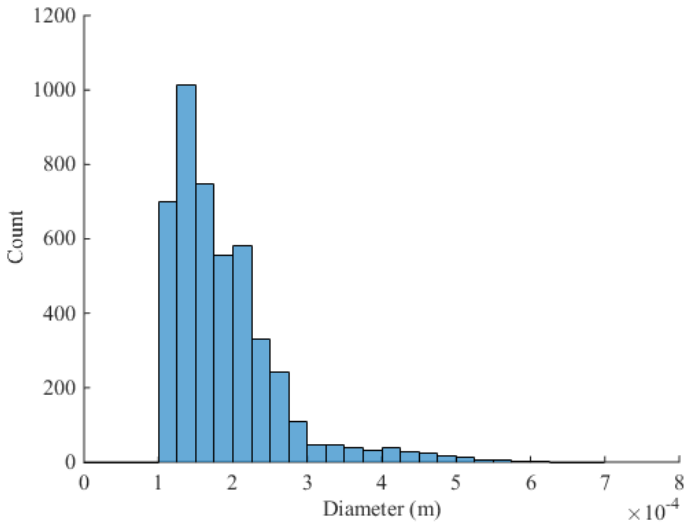

Figure 36: Measured drop size histogram

Examination of the measured particle displacements for this configuration in Figure 37 shows significantly more scatter in the Z direction, resulting in a Z positional uncertainty of 0.232 mm, one of the highest of all the data sets. Comparing this plot to those in other data sets gives a visual representation of the conclusion drawn previously that the increased uncertainty is a result of less scatter in the X direction since the Z scatter is not significantly larger than in other configurations. This indicates a limit on the Z positional uncertainty of the imaging system rather than a difference due to the configuration. It should also be noted that the linear fit lines for the X

and Z directions have extremely similar slopes in this data set, validating that the flow field was measured to be symmetric as expected.

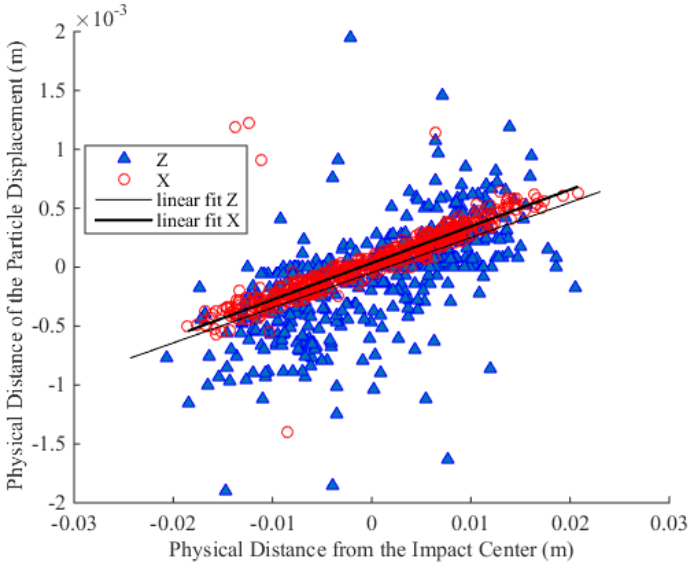

Figure 37: Measured particle displacements

3. *We = 624, τ = 6.7*

This configuration, which was the largest delay time tested for this Weber number, shows further increases in particle diameter distribution as well as Z positional uncertainty as shown in Figure 38 and Figure 39 respectively.

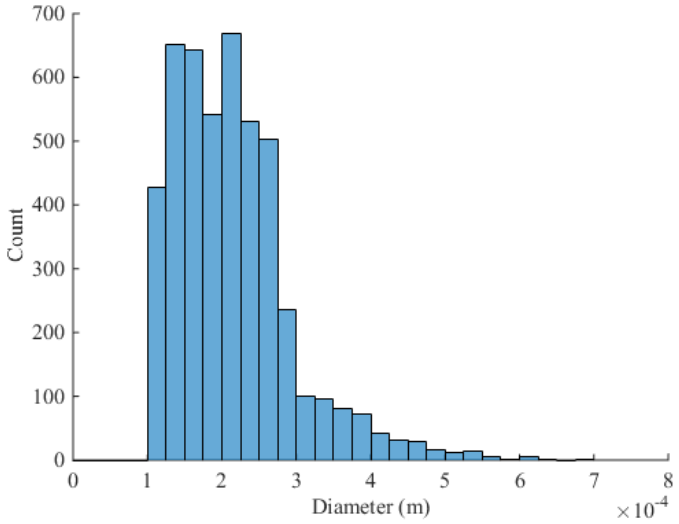

Figure 38: Measured drop size histogram

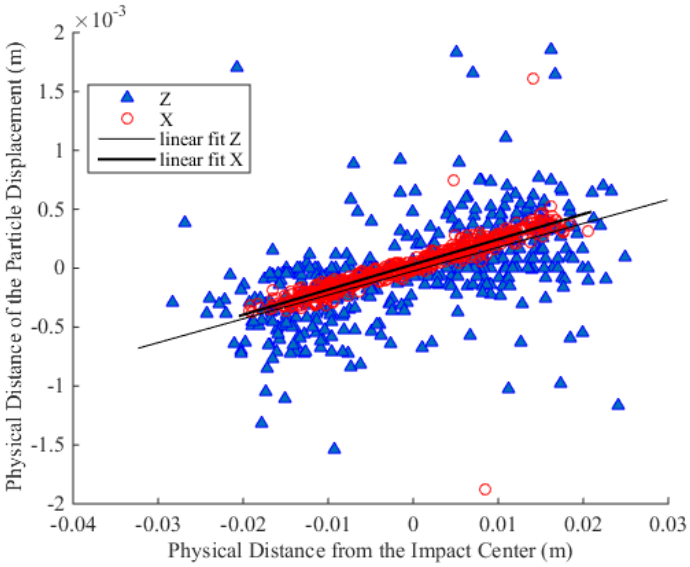

Figure 39: Measured particle displacements

4. We = 784, τ = 2.6

This configuration at an increased Weber number and again a smaller delay time produced results similar to those seen for a short delay time at the lower Weber number. The histogram shown in Figure 40 shows detected diameters generally ranging from 0.1-0.2 mm and an overall small number of particles.

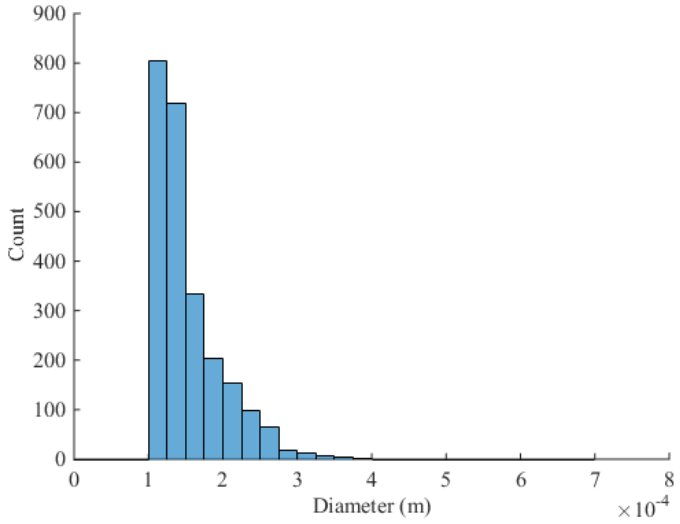

Figure 40: Measured drop size histogram

Figure 41 shows significant scatter in both dimensions resulting in a low Z positional uncertainty and some disagreement in the slopes of the linear fit lines, possibly indicating an inability to resolve these statistics with the given number of data points.

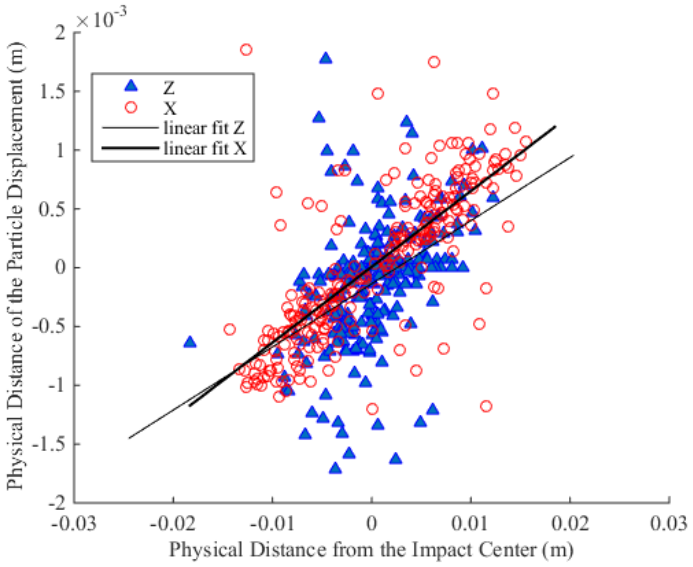

Figure 41: Measured particle displacements

5. We = 784, τ = 5.1

This is the experimental configuration shown as the example case in section VI.A.1. As the delay time at this higher Weber number is increased the same trends are apparent as at the previous Weber number. The drop size histogram in Figure 42 shows a significant number of particles between 0.1-0.3 mm in diameter and an overall large number of particles are detected.

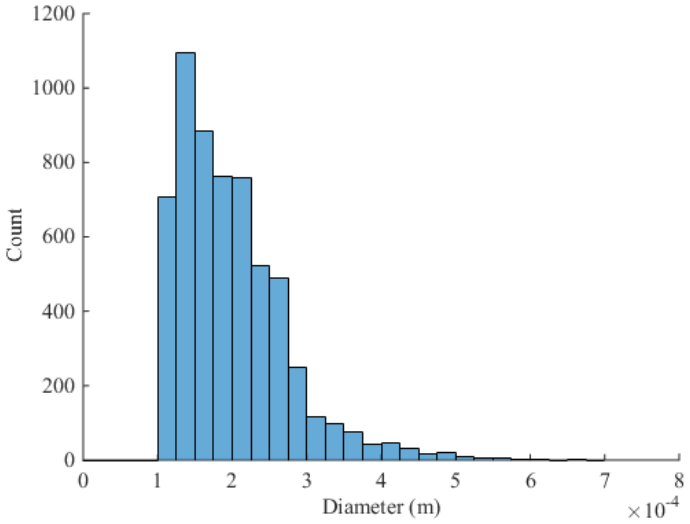

Figure 42: Measured drop size histogram

The measured particle displacements in Figure 43 show increased Z positional uncertainty and a reduction in the scatter in the X direction though there is still more scatter than at the lower Weber number and moderate delay time.

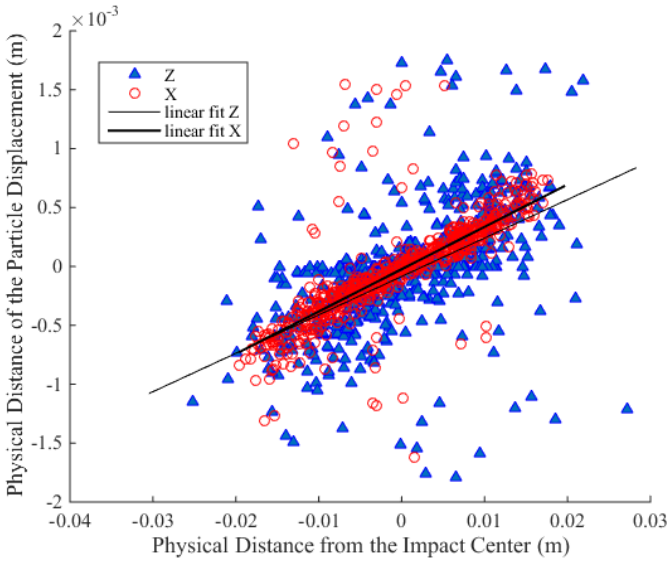

Figure 43: Measured particle displacements

6. *We = 784, τ = 7.7*

Following the previously discussed trends, this final configuration at the moderate Weber number and long delay time shows a significant number of particles detected at diameters ranging from 0.1 to over 0.4 mm in Figure 44 and increased Z positional uncertainty in Figure 45 as well as an overall large number of particles.

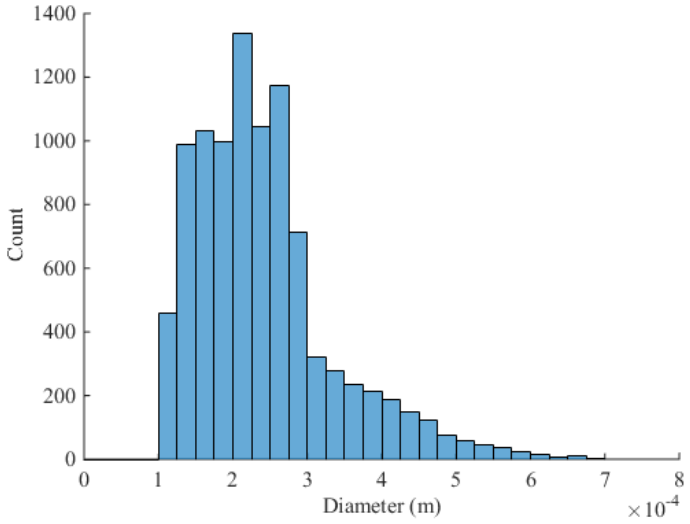

Figure 44: Measured drop size histogram

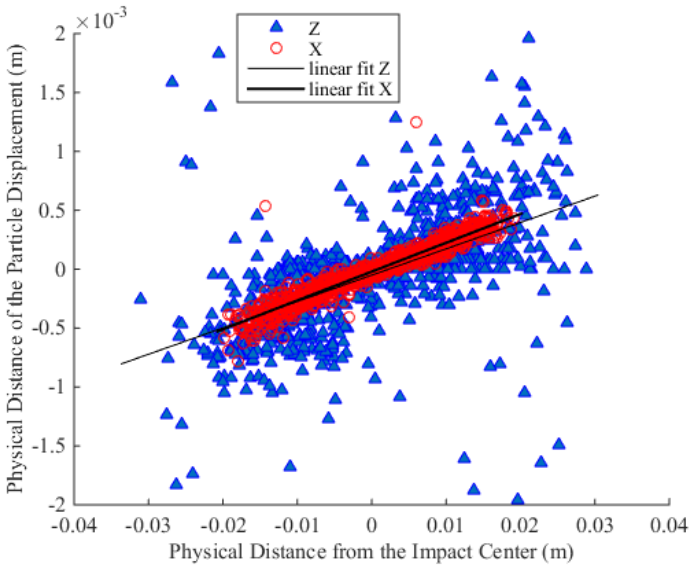

Figure 45: Measured particle displacements

7. We = 1051, τ = 3.0

Examination of this highest Weber number at a small delay time shows a slight increase in the diameters detected even at this first small delay time as shown in Figure 46.

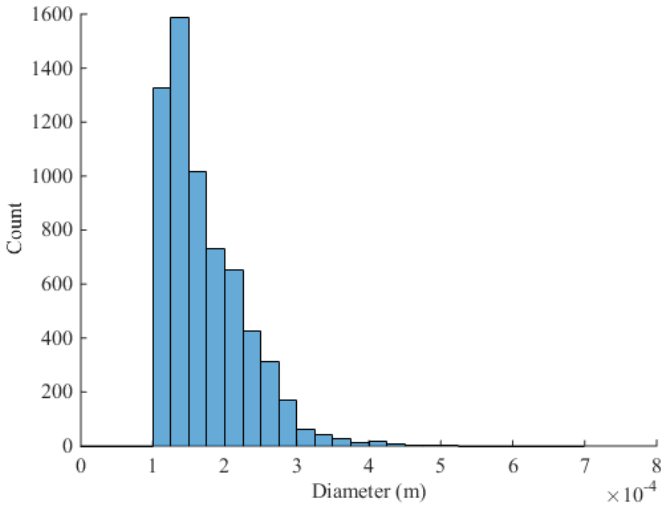

Figure 46: Measured drop size histogram

Figure 47 shows significant scatter in the measured particle displacements in both directions, but closer agreement of the linear fit line slopes than at the small delay times for the other Weber numbers.

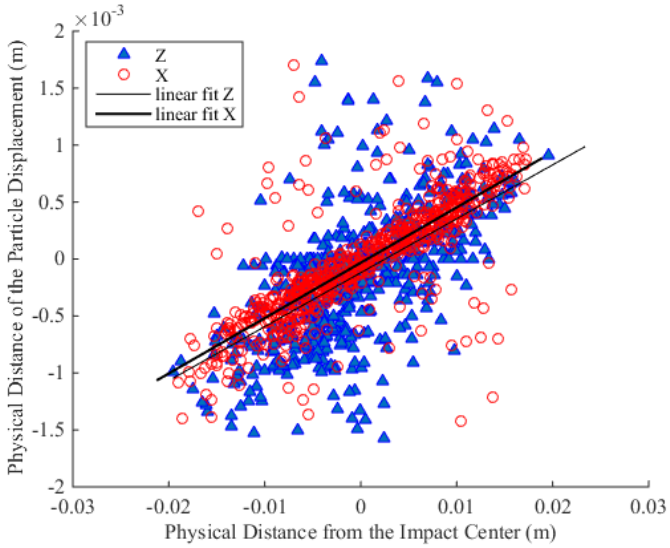

Figure 47: Measured particle displacements

8. We = 1051, τ = 6.0

At this high Weber number and moderate delay time a very large number of particles were detected and, as expected, the range of diameters increased as did the Z positional uncertainty as shown in Figure 48 and Figure 49 respectively.

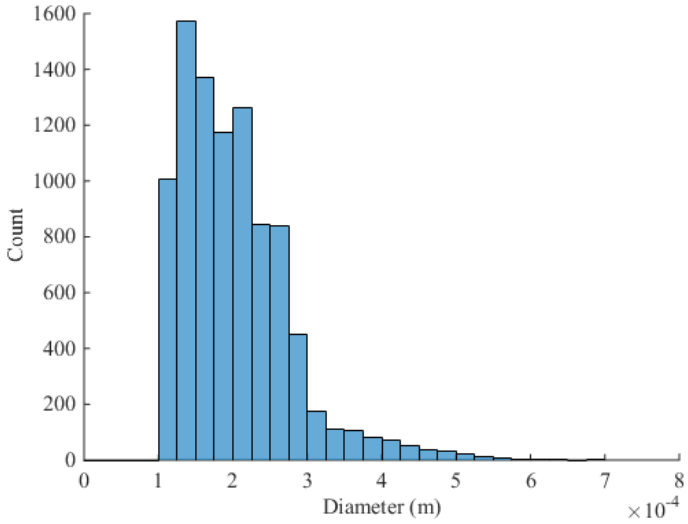

Figure 48: Measured drop size histogram

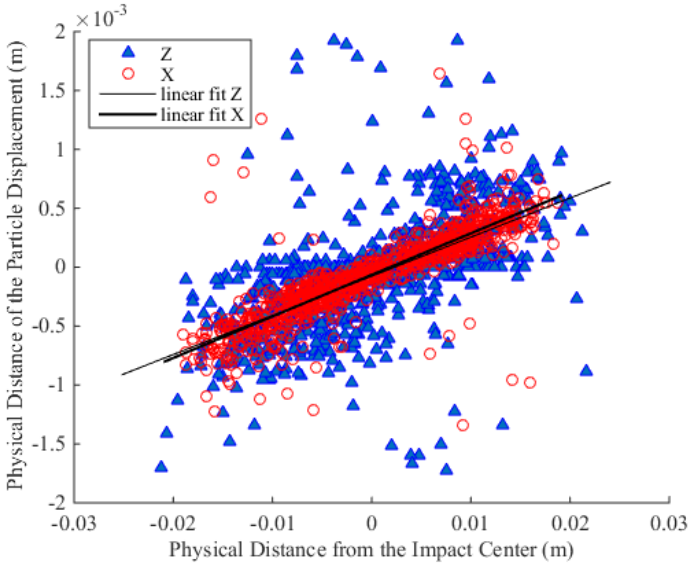

Figure 49: Measured particle displacements

9. We = 1051, τ = 9.0

The final experimental configuration, at a high Weber number and large delay time shows a relatively large range of particle diameters as in Figure 50 and a large Z positional uncertainty from Figure 51.

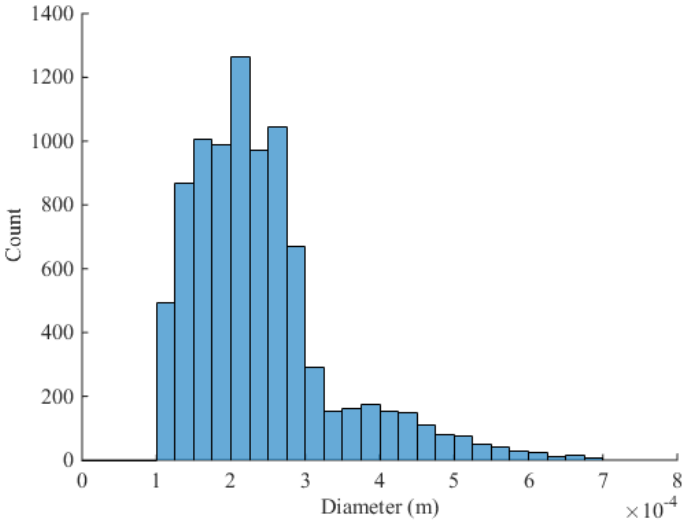

Figure 50: Measured drop size histogram

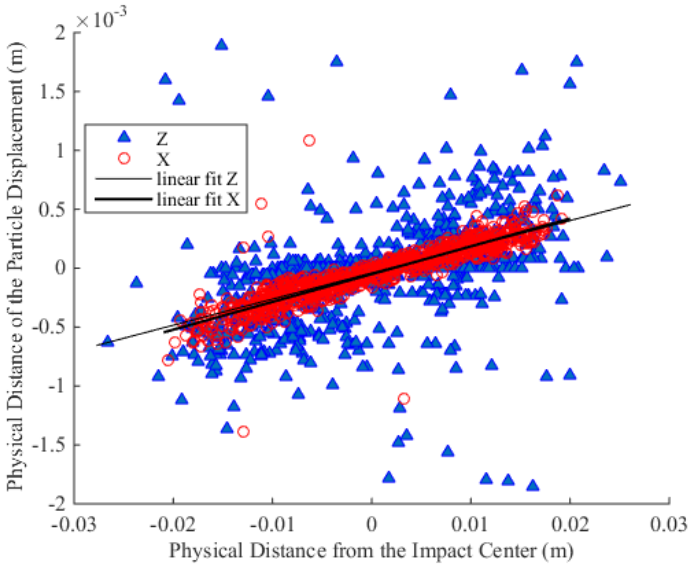

Figure 51: Measured particle displacements